Muhammad Riandy Eddy

Prediction of Stress Distribution using 3D Geomechanical Model in De Lier Field, the Netherlands

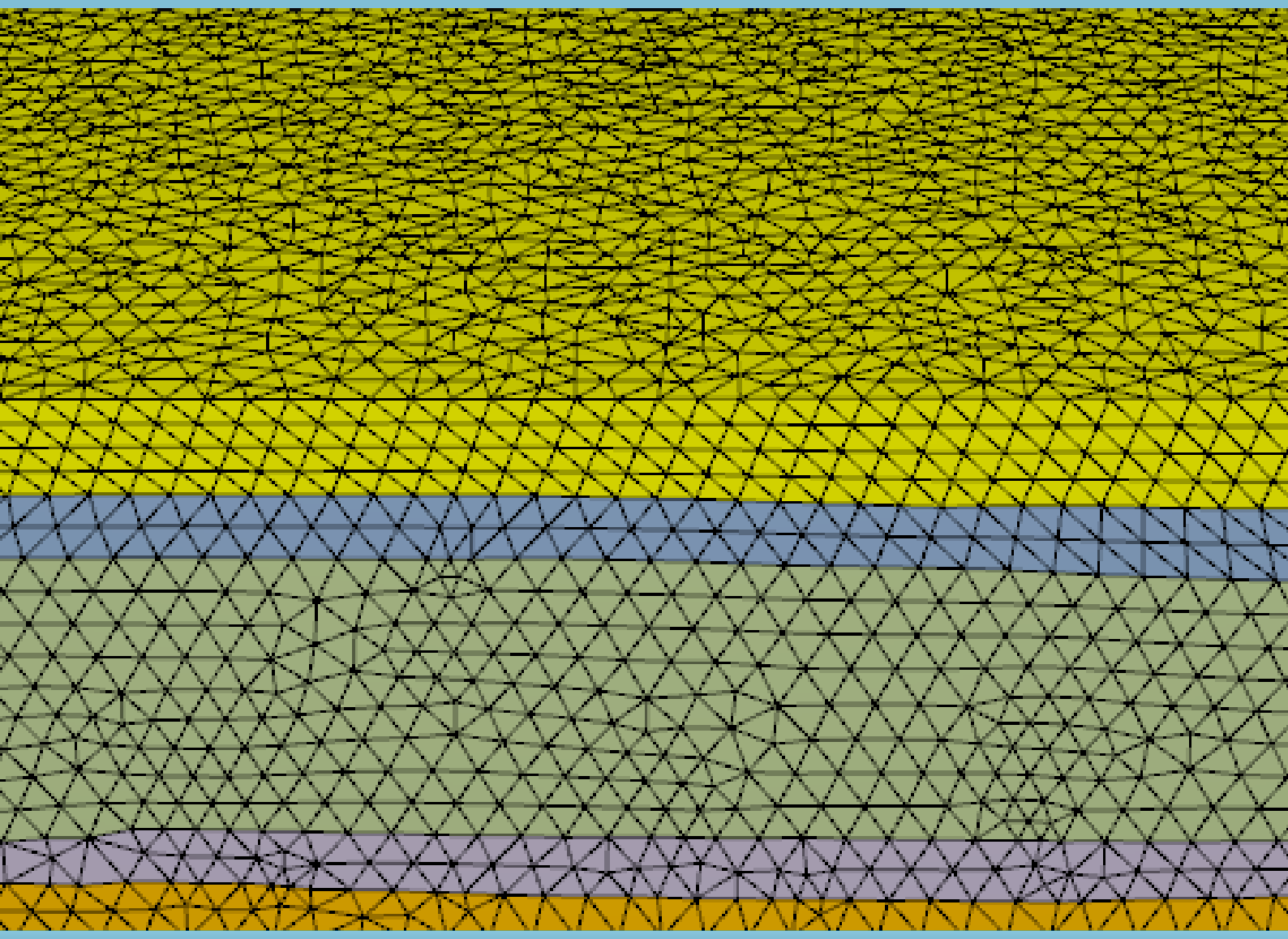

TU Delft

Prediction of Stress Distribution using 3D Geomechanical Model in De Lier Field, the Netherlands

By

Muhammad Riandy Eddy

in partial fulfilment of the requirements for the degree of

Master of Science
in Applied Earth Sciences

at the Delft University of Technology,
to be defended publicly on Monday November 20, 2017 at 09:30 AM.

Supervisor:	Prof. Dr. G. Bertotti	TU Delft
Thesis committee:	Dr. A. Barnhoorn,	TU Delft
	Drs. J.C. Blom,	TU Delft

TU Delft

Abstract

An understanding about geomechanical condition is necessarily needed in order to examine the state of stress of a subsurface area. Geomechanical modeling is one of the method to understand the mechanical condition and has been used in various subsurface-related industries such as oil and gas, geothermal, and CO_2 storage. The principal stress distribution influences the stress regime and dictates the creation of different type of fault and fracture. The magnitude and orientation of principal stresses are controlled by the physical and mechanical properties of the rock such as density and Poisson's ratio. It is also effected by the tectonic stress and the geometry of the model which is created using the seismic data. In the case where the gravity is the only source of stress in the model, normal stress regime is observed in the whole depth. Meanwhile, in the case of tectonic stress is also involved, the stress regime changes over the depth from reverse, strike-slip, to normal stress regime. Lateral variation of the stress magnitude is observed even though it is not really significant. The presence of the fault in the model does not have a large contribution to influence the magnitude and orientation of the principal stresses. Changing the pore pressure magnitude is indeed can affect the principal, effective stress, and the stress regime throughout the model.

Acknowledgement

Praise to God Almighty for all His blessing and protection.

First, I would like to express my sincere gratitude to my supervisor Prof. Giovanni Bertotti for all his guidance, patience, and advice during the process of this master thesis. Through his guidance and feedback, I could finally finish this master thesis which indicates the end of my master study in TU Delft. Thanks to Dr. Nico Hardebol for guiding me during the early stage of my master thesis including the knowledge about the Abaqus software and providing the JewelSuite software. To Dr. C.J.L. Willems, thanks for providing the necessary data. Special thanks to Rizki Wira Pradipta and Bagus Arief Wibowo from Baker Hughes for guidance about the JewelSuite software.

I also would like to thank the Indonesian Endowment Fund for Education (LPDP) for giving me the opportunity to pursuit my dream to study in one of the best university in the world by providing me a full financial support during the two-years master program.

I would like to dedicate my entire effort during my study to my beloved parents, my sister and her husband, my brother, my auntie, my entire Zubir's and Bey's family and also to the newest member of the family, Alula Lashira Aditya.

Last, I also would like to thank all my classmate in Petroleum Engineering and Geosciences and Indonesian Student Association in Delft for their friendship and supports during my journey in the Netherlands. Special thanks to my fellow residents in The Student Hotel Den Haag, Valkenlaan 36, and Bosboom Toussaintplein 28 Delft. It is an honour to share a life with you.

Muhammad Riandy Eddy,

Delft, 10 November 2017

Table of Contents

List of Figures

List of Tables

1. Introduction

1.1. Background

An understanding about geomechanical condition is necessarily needed in order to examine the state of stress of a subsurface area. The geomechanical modeling is the method to understand the mechanical condition in the subsurface. This method can be applied in several purposes of study including the hydrocarbon, geothermal, and environmental study such as carbon capture and storage. Using this method, a knowledge of state of stress within an area can be achieved. The knowledge about the stress condition is very important for instance in performing drilling activities. Study of wellbore stability, hydraulic fracturing, and fluid injection are the examples of the study in hydrocarbon and geothermal that related with drilling activities. Meanwhile, the utility of the geomechanical modeling in carbon capture and storage is quite similar with the application in hydrocarbon and geothermal study. Since the concept of the carbon capture and storage is similar with fluid injection in hydrocarbon and geothermal study.

The development of geological structure such as fault and fracture in the subsurface area is occurred as a response from the combination of the magnitude and direction of the principal stresses. Variation of stress regime along the depth and in a certain area can lead into a construction of different type of fault and fracture. Combination of the knowledge about the state of stress and the fault pattern within a field is important to decide the well location, orientation, and direction for instance in the geothermal doublet. Mostly the direction of the geothermal doublet is parallel with the fault and fracture since they possibly can increase the permeability of the rock itself and most likely become the fluid flow path. This is similar with the case of placing and positioning the injection and production well in the hydrocarbon drilling activity where the pattern of the fault and stress condition are the major factors that have to be considered and evaluated.

In this study, the geomechanical model is built using the data from the geothermal field, De Lier, the Netherlands. De Lier field located in the Westland area, Zuid-Holland province has become one of the prominent geothermal field in the Netherlands. De Lier field is sited in the West Netherlands Basin and the location of this onshore geothermal field has been studied since late 70's. The feasibility study for Delfland project has been carried out and suitable for installation of geothermal doublet. In the earlier study of this location, the primary aquifer target of this field is belong to the Vlieland Formation, Rijnland Group (Walter, 1995) because plenty amount of data is available from oil and gas exploration. But recently, Nieuwerkerk Formation, Schieland Group from Lower Cretaceous is also becoming another target of geothermal aquifer in this field.

1.2. Objective

The aim of this study is to build a 3D geomechanical model in the De Lier field, the Netherlands using the available data such as seismic and well data with their limitation (further explain in chapter 3). The 3D geomechanical model is used to predict the state of stress in the De Lier field. This 3D model contains the three-dimensional stress distribution with the involvement of the overburden and tectonic stress as the source of stress. Several stress scenarios are applied to the 3D geological model in order to generate the 3D stress distribution. Through the generation of the model, the principal stresses magnitude and orientation can be determined. The stresses in a certain direction can also be extracted from the 3D geomechanical model.

2. Literature Study

2.1. Regional Geology

West Netherlands Basin is located in the Netherlands and southern part of the North Sea with NW-SE orientation. It is bordered with Central Netherlands Basin in the North East and London-Brabant Massif in the South West as shown in Figure 1. Mid Netherlands Fault Zone with NW-SE orientation is the boundary between West and Central Netherlands Basin. The West Netherlands Basin was created during the Late Jurassic and the Early Cretaceous rifting phase as a series of half-graben with NW-SE orientation (Wong, Batjes, & Jager, 2007).

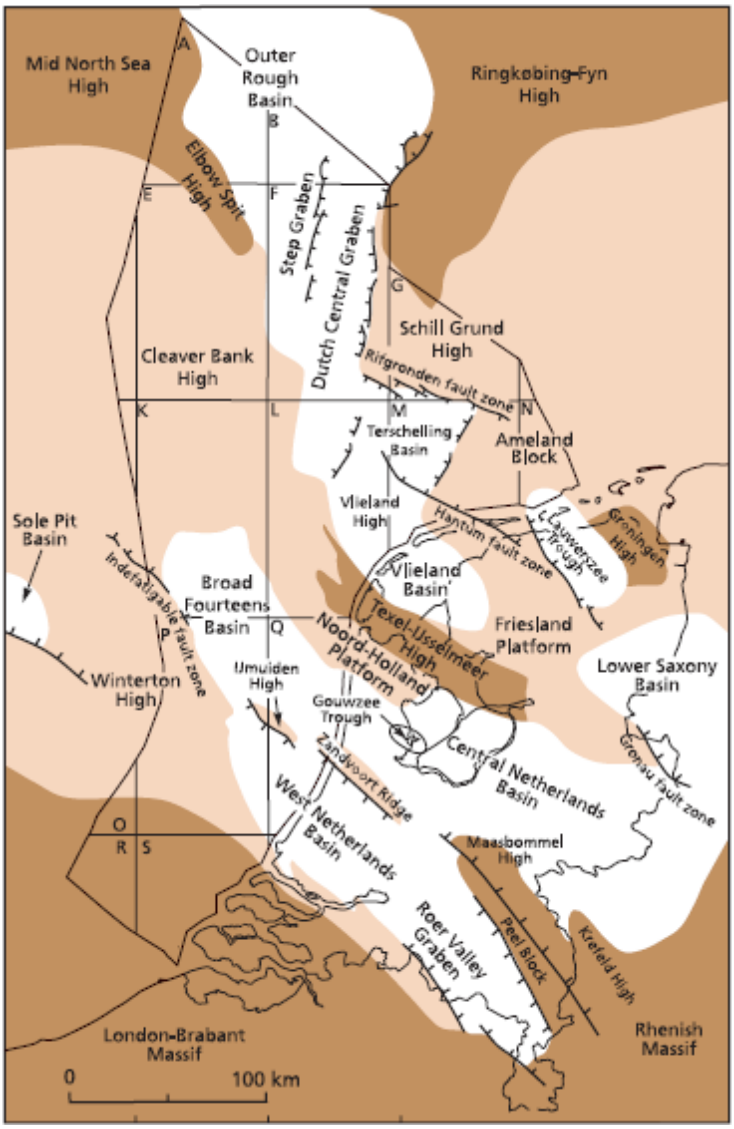

Figure 1. Upper Jurassic and Lower Cretaceous structural map in the Netherlands (Van Adrichem Boogaert & Kouwe, 1993-1997). White: Basin; light brown: intermediate high and platform; dark brown: high structure platform (Wong, Batjes, & Jager, 2007).

The break-up of Pangea supercontinent were occurred during the Mesozoic resulting the major rifting phase called Kimmerian tectonic phase. The extensional tectonic force during this process was oriented to E-W direction, created the half-graben structures in the West Netherlands Basin with NW-SE orientation. The difference of this orientation was assumed because there was another factor controlled this formed structure such as the pre-existing

structural feature reactivated. Large rifting event in the Late Jurassic and Early Cretaceous divided some basins into several blocks of graben. Abundant fault zones were formed due to this large and extend rifting period.

During the Late Cretaceous and Early Tertiary, Alpine inverted because of the collision of the African and European Plate. The orientation of the maximum stress of this compressional regime from Alpine Orogeny was NNW and oblique to the NW-SE faults in the West Netherlands Basin and re-activated the pre-existing faults. Therefore, the transpressional movements created a set of flower structure with NW-SE orientation. Moreover, the inverted part of the basin mostly eroded during the Oligocene.

The Cretaceous period in the Netherlands was divided into several subdivisons (Wong, Batjes, & Jager, 2007). Schieland Group, Delfland Subgroup lying from Oxfordian until Barremian was filled with siliciclastics and continental deposits. One dominant formation was formed in this group, Nieuwerkerk Formation. Rijnland Group from the Barremian until Albian deposited the marine deposits due to the sea level rise and transgression to the landward. This group was divided into Vlieland Sandstone and Mudstone Formation and Holland Formation. The last group was Chalk Group in the Upper Cretaceous and Danian. Texel Formation, Ommelanden Formation, Ekofisk and Chalk Group in the Southern Netherlands are the formations categorized in this group.

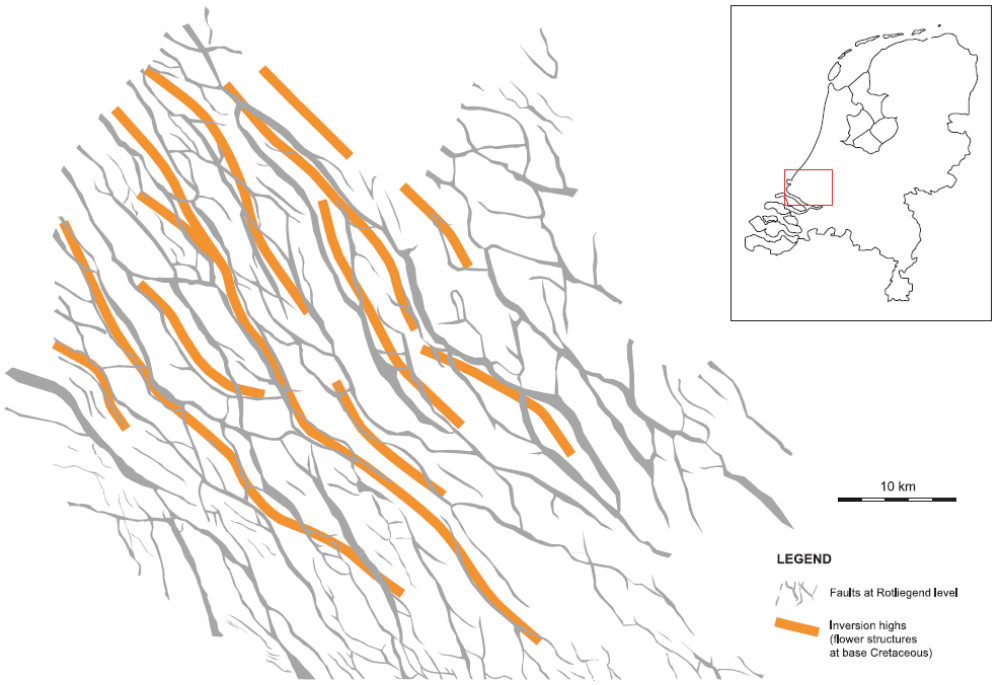

Figure 2. Fault pattern at Rotliegend (Permian) with WNW-ESE and NNW-SSE faults direction (grey lines) and continuous flower structures at Base Cretaceous (orange line) (Wong, Batjes, & Jager, 2007).

The two groups in the West Netherlands Basin, Schieland and Rijnland Group were stated as the good reservoir for geothermal energy (Vis, et al., 2010). However, in this study, the discussion is more focus on the Schieland Group, where the Nieuwerkerk Formation, De Lier field geothermal reservoir is located.

The Nieuwerkerk Formation was deposited in the syn-rift of Lower Cretaceous and post-rift phase as fluvial unit in West Netherlands Basin. It was consisted of Alblasserdam, Delft Sandstone and Rodenrijs Claystone member based on (Van Adrichem Boogaert & Kouwe, 1993-1997). The oldest member of this formation was Alblasserdam member while the youngest was Rodenrijs Claystone. Due to this formation was deposited in the fluvial environment, it was known with its heterogeneity and discontinuous reservoir layer. The thickness of this formation can reach out 1 km.

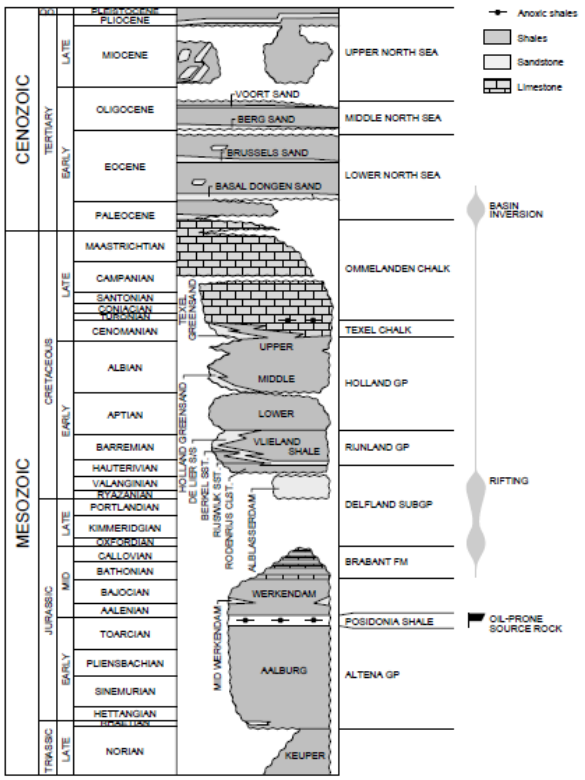

Figure 3. Tectonostratigraphy of Nieuwerkerk Formation, West Netherlands Basin (DeVault & Jeremiah, 2002).

The upper boundary of this formation was the Rijnland Group onlapping to this formation and in the southern basin margin. The lower boundary of this formation was the Altena Group. The boundary between them was an unconformity. The Altena Group was mainly consisted of claystones and sandy carbonates.

The lithology of this formation is fine-to medium-grained sandstone, coarse-grained thick bedded sandstone, and red and grey claystone. It is also found the coal beds related with grey claystone. Mottling is identified in several claystone layers derived from a core sample. The sandstone layers are isolated, sheet-like and stacked channel resembles the fluvial environment either braided river or meandering river. The claystone interpreted to be deposited as the crevasse splays in a floodplain.

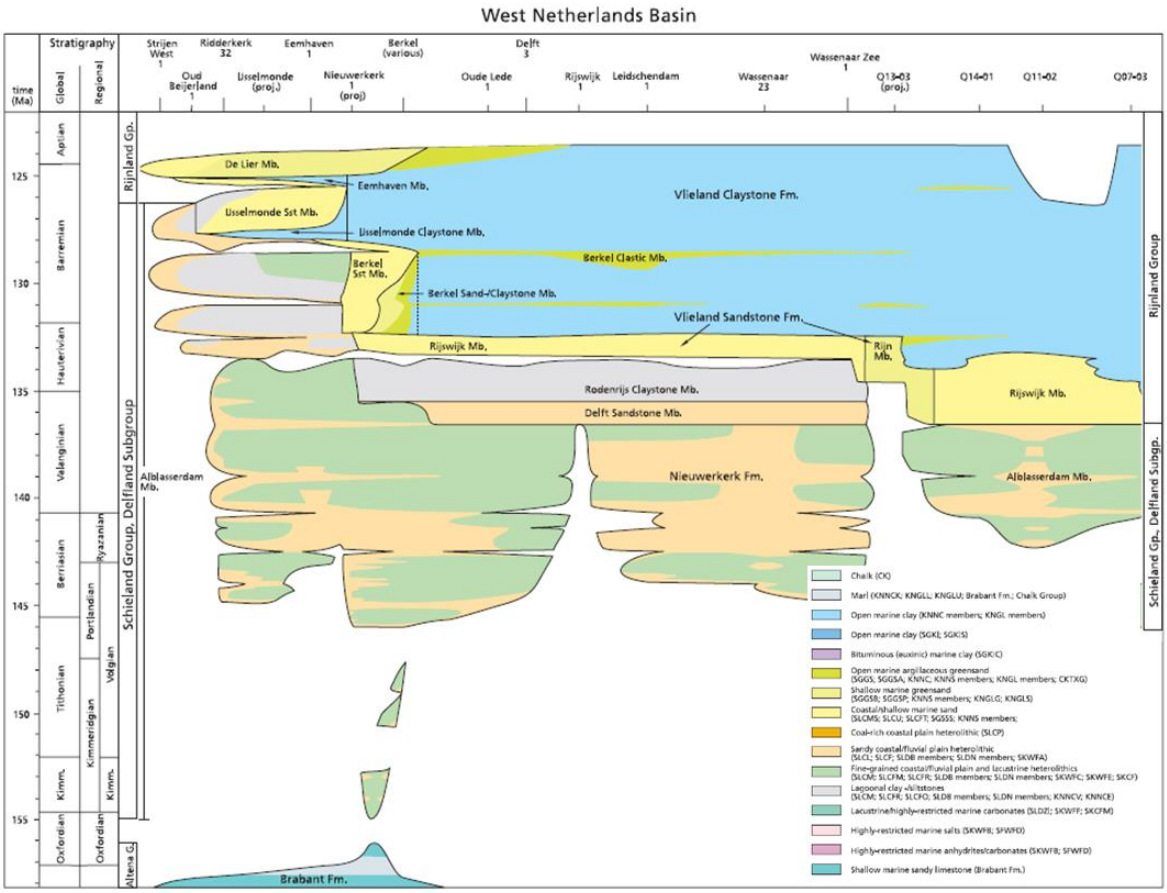

Figure 4. Stratigraphic Scheme of West Netherlands Basin (Wong, Batjes, & Jager, 2007).

2.2. Basic Theory of Geomechanics

Geomechanical model and simulation was prepared by calculating the state of stresses. State of stress is a tensor consisted of the stress components. The basic definition of the stress itself is simply the force per given area. In a Cartesian coordinate system, stress tensor is defined as shown in equation below (Zoback M. D., Reservoir Geomechanics, 2007),

$$S = \begin{bmatrix} S_{11} & S_{12} & S_{13} \\ S_{21} & S_{22} & S_{23} \\ S_{31} & S_{32} & S_{33} \end{bmatrix}$$

The subscripts shown in each of matrix component above sometimes are also written as x, y, and z instead of 1, 2, and 3, respectively. Each of these subscripts represent the axis of an arbitrary Cartesian coordinate system and the direction of the acting stresses.

The component of the stress on an arbitrary Cartesian coordinate system can be transformed into another coordinate system. For example, transforming the Cartesian coordinate system to the principal coordinate system is a common practice. Describing the state of stress using the principal coordinate system is easier and simpler since in this coordinate the shear component of stress is described as zero. The surface of the earth is described as one of the principal plane since it has contact with fluid (either water or air) which cannot sustain the shear stress component. Therefore, one of the principal stress direction is normal to the surface of the earth while the other two principal stress direction are about at horizontal direction (Zoback M. D., Reservoir Geomechanics, 2007). The stress tensor in the principal plane coordinate system (S') can be found in the equation below,

$$S' = \begin{bmatrix} S_1 & 0 & 0 \\ 0 & S_2 & 0 \\ 0 & 0 & S_3 \end{bmatrix}$$

The S_1, S_2, and S_3 are the maximum (greatest), intermediate, minimum (least) principal stress, respectively. Since they are principal stresses, there are no shear stresses acting on the principal planes.

In order to fully evaluate state of stress, there are at least 4 parameter that must be determined. The vertical stress, S_v (overburden stress); the maximum horizontal stress, (S_{Hmax}); minimum horizontal stress (S_{hmin}); and one stress orientation such as azimuth of maximum horizontal stress. The calculation of the vertical stress is using the equation below,

$$S_v = \int_0^z \rho(z)\, g\, dz = \rho * g * z$$

where:

- S_v is vertical stress (Pa)
- ρ is the density of the overburden rock (kg/m^3)
- g is gravitational acceleration (m/s^2)
- z is depth from surface to a particular depth (m)

The calculation of horizontal stresses are using the equation below (Bertotti, et al., 2017),

$$S_{hmin} = \left(\frac{v}{1-v}(\rho g z - \alpha P_p)\right) + \left(\frac{v}{1-v}(S_{tect})\right) + (\alpha P_p)$$

$$S_{Hmax} = \left(\frac{v}{1-v}(\rho g z - \alpha P_p)\right) + S_{tect} + (\alpha P_p)$$

where:

- S_{hmin} is minimum horizontal stress (Pa)
- S_{Hmax} is maximum horizontal stress (Pa)
- v is Poisson's ratio (-)
- S_{tect} is tectonic stress (Pa)
- α is Biot's coefficient (-)
- P_p is pore pressure (Pa)

The first term from this formula is a linear elastic term that transform the vertical stress to the horizontal stress on the rock. The second term is about the external source of stress such as the tectonic stress. And the third term characterizes the fluid pressure in the pore of the rock.

To determine and extract the stress orientation and magnitude at present day including the tectonic stress information, there are several geological and geophysical types of data usually used such as wellbore breakouts, earthquake focal mechanism, *in-situ* stress measurements (hydraulic fracturing and overcoring stress measurement), fault slip data and volcanic vent alignments (Zoback M. L., 1992). For example, the tectonic stress can be obtained by comparing the measured horizontal stress with the horizontal stress calculated from the equation above.

Primary source of the horizontal stress in Western Europe where the West Netherlands Basin located is the ridge push of European Plate and continental collision with African Plate (Zoback M. L., 1992). The maximum horizontal stress is oriented uniformly at NW to NNW with mean azimuth value of N145ºE±26º (Muller, et al., 1992).

Based on the E.M. Anderson's faulting theory as it is shown in Table 1, the magnitude of the vertical, maximum horizontal and minimum horizontal stress are influencing the faulting regime. If the vertical stress becomes the largest principal stress, the normal faulting regime would likely be occurred. Meanwhile, if the vertical stress becomes the least principal stress, the reverse faulting regime would possibly be happened. The strike-slip faulting regime is the condition where the vertical stress is larger than minimum horizontal stress but not larger than maximum horizontal stress.

Stress regime	**Stress**		
	S_1	**S_2**	**S_3**
Normal faulting	S_v	S_{Hmax}	S_{hmin}
Strike-slip faulting	S_{Hmax}	S_v	S_{hmin}
Reverse faulting	S_{Hmax}	S_{hmin}	S_v

Table 1. Stress faulting regimes with principal stresses and its corresponding stress orientation.

Since S_{hmin} is always smaller than S_{Hmax}, only the vertical stress and maximum horizontal stress might become the S_1.

When a porous rock is subjected by a stress, there is a counter pressure from fluid inside the pore space of the rock itself. This fluid pressure is called pore pressure. The concept of effective stress was introduced by Karl Terzaghi. It is said that in the poroelastic material behaviour, the difference between the total stress and pore pressure is effective stress. The stress felt by the grains actually is not only the external stress but the effective stress which in here includes the pore pressure (Terzaghi, 1943).

$$\sigma = S - P_p$$

Where the σ is effective stress (can be horizontal or vertical), S is total stress, and P_p is pore pressure.

One of the way to obtain the magnitude of pore pressure is using the relation between the porosity and the effective vertical stress (Zoback M. D., Reservoir Geomechanics, 2007),

$$\varphi = \varphi_0 e^{-\beta\sigma_v}$$

Where the φ is porosity, β is empirical constant, σ_v is effective vertical stress. The porosity data can be obtained from geophysical data such as sonic or resistivity log and vertical stress (S_v) is calculated using the previous formulation above. Thus, the magnitude of pore pressure can be calculated since it is the only unknown variable here.

The ratio between the effective horizontal and vertical stress is called effective stress ratio. The effective stress ratio formula based on minimum horizontal stress can be seen in equation below (van der Zee, Ozan, Brudy, & Holland, 2011),

$$ESR_{min} = \frac{S_{hmin} - P_p}{S_v - P_p} = \frac{\sigma_{hmin}}{\sigma_v}$$

And for effective stress ratio based on maximum horizontal stress,

$$ESR_{max} = \frac{S_{Hmax} - P_p}{S_v - P_p} = \frac{\sigma_{Hmax}}{\sigma_v}$$

The positive ESR means that the horizontal stress has a greater magnitude than the vertical stress. This effective stress ratio is very important in building and simulate the stress in geomechanical model since it is one of the parameter input for geomechanical model and simulation that is explained in later chapters.

Based on the geological stress convention, positive stress means compression and negative stress is tension. Meanwhile, the engineering stress convention represents the positive stress as tension and negative as compression. On the following chapter, there are two softwares mentioned in order to create the geomechanical model. JewelSuite 6.2 Subsurface Modeling from Baker Hughes and Abaqus/CAE (Complete Abaqus Environment) from Dassault Systèmes. The JewelSuite is using the geological stress convention while the Abaqus using engineering stress convention.

3. Datasets

In this study, geomechanical modeling was performed using several datasets as the input. Seismic and well data were the main input for the modeling.

3.1. Seismic Data

The geometry of the geomechanical model was created from the geological horizons and faults. In order to achieve those data, seismic data were needed. Based on the location of the study, the seismic data was the 3D onshore seismic data located on the southwest of the Netherlands where the De Lier field sited. The seismic data used in this study was the L3NAM1990C. It was a 3D time migrated seismic data and obtained from www.nlog.nl. This seismic data was cropped into a sub-volume. The location of the sub-volume was chosen due to the structural features in that sub-volume. The geomechanical model was built based on this seismic sub-volume. The location of full volume of L3NAM1990C seismic data and its sub-volume can be seen in Figure 5 and the detail description in Table 2. The area of the sub-volume of L3NAM1990C was reduced into around 72 km^2 from the full volume which was around 791 km^2. The length of sub-volume of L3NAM1990C was oriented to the N128^{o}E.

Figure 5. Base map of L3NAM1990C overlain with map of the Netherlands. Black box was the full volume of L3NAM1990C and the red box was the sub-volume of L3NAM1990C.

Description	Value (Full Volume)	Value (Sub-Volume)
Number of inlines	1921	601
Number of crosslines	1031	301
Inline range	580 – 2500	1130 – 1730
Crossline range	110 – 1140	700 – 1000
Inline interval	20 m	20 m
Inline length	20601.52 m	6000.44 m
Crossline interval	20 m	20 m
Crossline length	38396.75 m	11998.98 m

Table 2. Detail description of full volume and sub-volume of L3NAM1990C.

Two horizons were interpreted in time domain from the sub-volume of L3NAM1990C seismic data, Base of Rijnland and Base of Schieland Group. The surface or the datum was also generated from this seismic data. The other group/formation horizons were obtained from www.nlog.nl. The geothermal aquifer of the De Lier field, Nieuwerkerk Formation is located in the Schieland Group.

The summary of the horizons and where they were taken can be seen in Table 3. The surface / top of the North Sea Group was considered as a flat land surface.

Horizons	Sources	Domain from www.nlog.nl
Surface / Top of North Sea Group	3D seismic data (L3NAM1990C)	-
Base of North Sea Group / Top of Chalk Group	www.nlog.nl	Time and depth
Base of Chalk Group / Top of Rijnland Group	www.nlog.nl	Time and depth
Base of Rijnland Group / Top of Schieland Group	3D seismic data (L3NAM1990C) and www.nlog.nl	Depth
Base of Schieland Group / Top of Altena Group	3D seismic data (L3NAM1990C) and www.nlog.nl	Depth

Table 3. Summary of horizons used in geomechanical modeling and their sources.

As an input of geomechanical model, the horizons and faults was needed to be on the depth domain. To convert the 3D seismic data in time domain to depth domain, the velocity model was needed. In chapter 4.1, it was described how the velocity model was obtained.

3.2. Well Data

There were 4 wells data used in this model, namely LIR-GT-01, LIR-GT-02, HON-GT-01 and HON-GT-02 and each of the wells had geological markers. The wells and markers were acquired from www.nlog.nl. Availability list of markers for seismic interpretation and the properties of the wells can be found in Table 4. And Table 5, respectively. The Figure 6 are showing the well location with respect to the seismic data.

Horizons	Markers
Surface / Top of North Sea Group	Not available
Base of North Sea Group / Top of Chalk Group	Available
Base of Chalk Group / Top of Rijnland Group	Not available
Base of Rijnland Group / Top of Schieland Group	Available
Base of Schieland Group / Top of Altena Group	Not available

Table 4. Horizons with their availability markers.

Well	X Coordinate	Y Coordinate	Well datum name	Well datum value [m]	TVDSS [m]	Measured depth [m]
HON-GT-01	75245.03	448075.03	KB	0	2944.0	3240.0
HON-GT-02	75235.02	448070.02	KB	0	2735.6	3041.0
LIR-GT-01	79087.74	443732.35	RT	4.8	2570.7	2897.0
LIR-GT-02	79090.03	443734.03	RT	5	2541.0	2880.0

Table 5. Properties of well data. KB = Kelly Bushing, RT = Rotary Table, TVDSS = true vertical depth – reference depth.

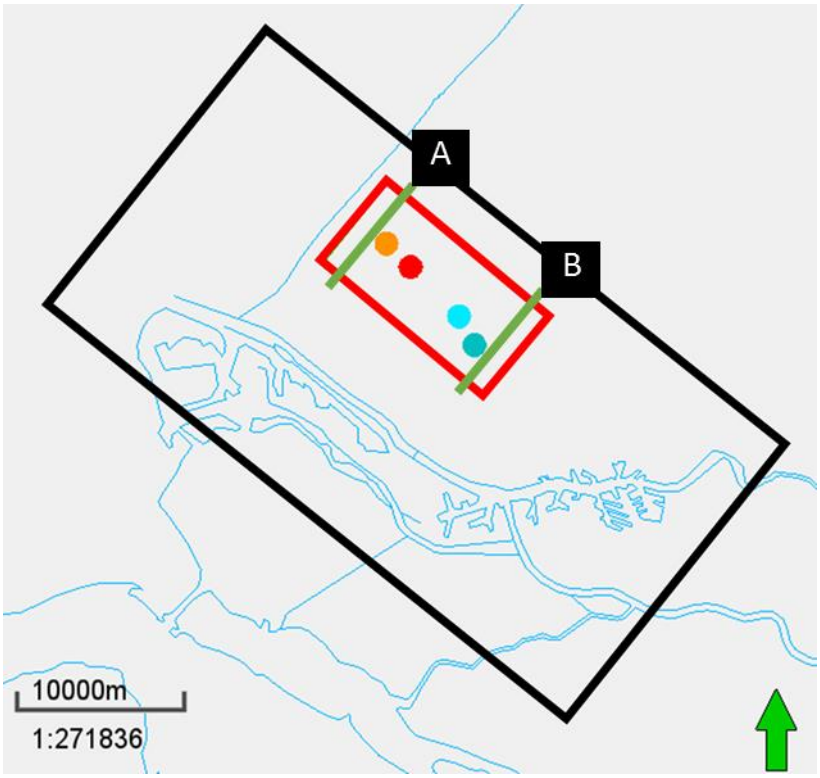

Figure 6. Well location with respect to the seismic data location. Black box = full volume of L3NAM1990C, red box = sub-volume of L3NAM1990C, orange dot = HON-GT-01, red dot = HON-GT-02, turquoise dot = LIR-GT-01, dark blue dot = LIR-GT-02. Green line A = inline 1240, green line B = inline 1650.

4. Methodology

4.1. Seismic Interpretation

Seismic interpretation was performed using the datasets mentioned in the previous chapter. Petrel 2014 software was used to execute the seismic interpretation. The seismic interpretation was performed by combining the seismic and well data in order to obtain the horizons and faults in the De Lier geothermal field.

First, the seismic-well tie was conducted. It was very important step since the seismic and well data were in the different domain, seismic data was on the time domain and the well data was on the depth domain. The well data used in this process were the markers of base stratigraphic unit from each wells. The missing markers (see Table 4) were replaced by the depth-domain horizons obtained from the www.nlog.nl. With the combination of these data, the seismic-well tie was able to be completed.

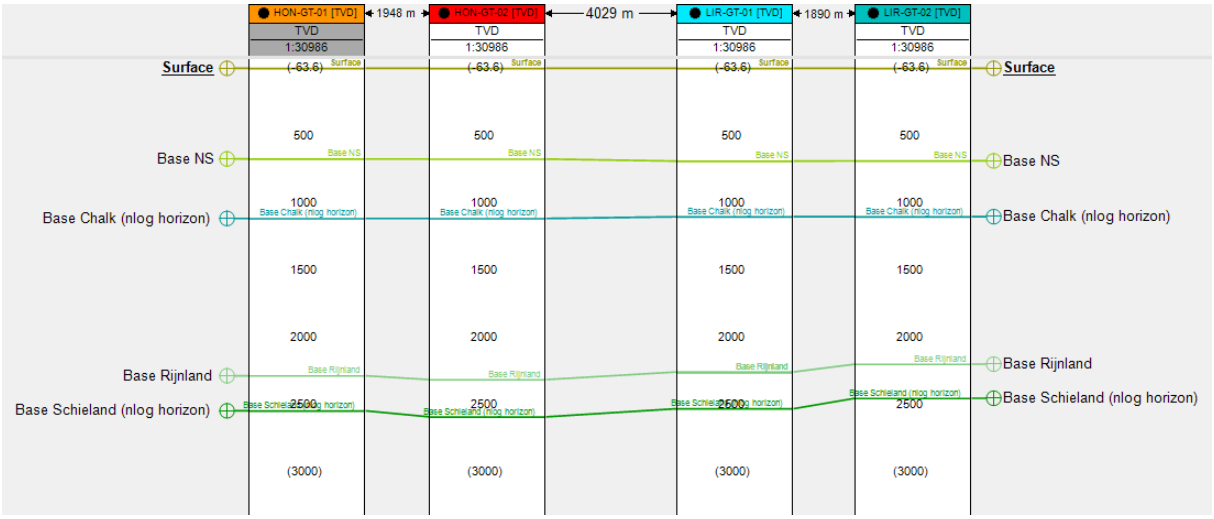

Figure 7. Geological markers from each wells with their corresponding depths.

Once the seismic-well tie was finished, the horizons and faults picking can be performed. Two horizons were picked, Base of Rijnland and Base of Schieland Group since the Schieland Group where geothermal aquifer of De Lier field located (Nieuwerkerk Formation) were bounded by these horizons. Because of some data limitations such as the checkshot and geological markers, horizon interpretation was performed using the available markers and lithostratigraphic information. The lithological contrast between the formations allowed the interpretation possible since it was resembled in the seismic. The lithostratigraphic information was obtained from the www.dinoloket.nl where the lithology, upper and lower boundary of each formations, and the geological feature between the two adjacent stratigraphic units were provided. Meanwhile, fault interpretation was interpreted directly using seismic section.

After the horizons and faults were obtained in time domain, in order to do the conversion to depth domain, the velocity model was required. The velocity model was determined based on layer cake depth conversion method. The definition of layer cake velocity model is a velocity model which each stratigraphic unit/formation has its own constant interval velocity. The input for the velocity model was the time-domain horizons and the markers from the well.

The velocity interval was determined based on trial and error with the 4 depth-domain known horizons from www.nlog.nl. They were compared with the input time-depth converted horizons. The goal was to make these input horizons matched with the existing horizons (horizons from www.nlogl.nl) in depth domain and also the markers. If they matched then the velocity model

was considered acceptable. Once the velocity model obtained, the time depth conversion can be applied to the horizons and faults. These depth-domain horizons and faults were the final output of the seismic interpretation can be proceeded to the next process as explained in chapter 4.2.

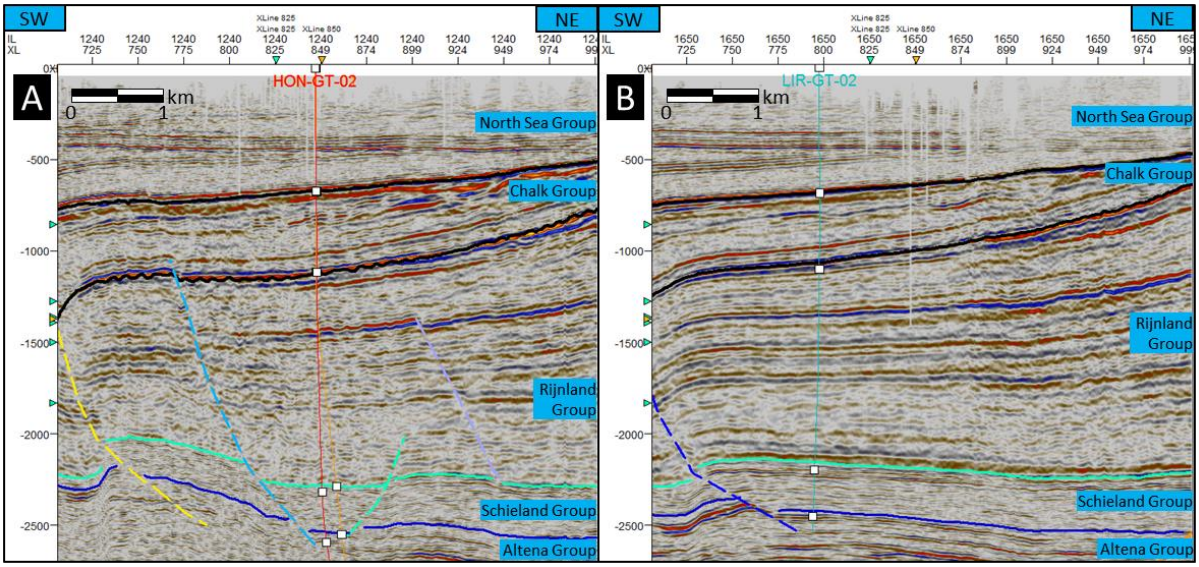

Figure 8. Seismic interpretation of horizons and faults in depth domain. The location of these seismic section was mentioned in Figure 6.

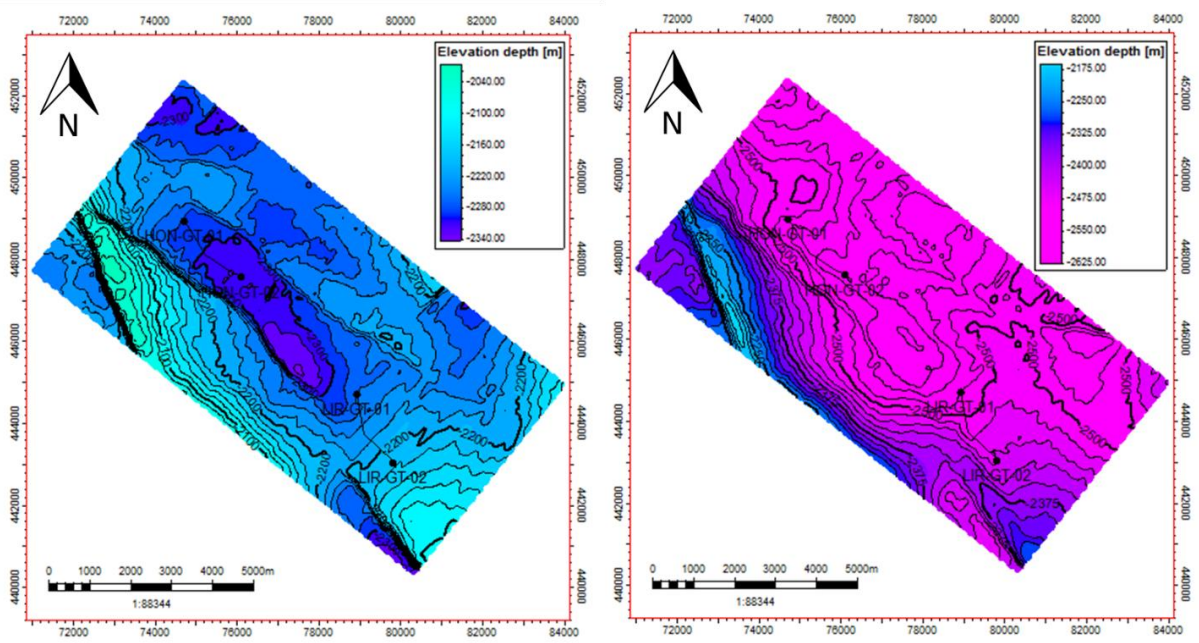

Figure 9. Base of Rijnland (left) and Schieland (right) depth contour after horizon picking and time-depth conversion.

Figure 8 is an example of horizons and faults interpretation in inline 1240 and 1650 with the interpreted formation/group. Meanwhile, Figure 9 is the interpreted Base of Rijnland and Base of Schieland Group. It can be seen that the Base of Rijnland is located from depth 2020 m to 2340 m while the base Schieland from 2175 m to 2625 m.

Some uncertainty might be included in the process of interpreting the seismic data. Mainly this is due to the seismic-well tie was performed without the checkshot data. The incomplete markers can also become the reason that leading the larger uncertainty especially when picking the horizon.

4.2. 3D Geological Modeling

As the output of seismic interpretation, the horizons and faults in depth domain were imported to JewelSuite software. JewelSuite 6.2 Subsurface Modeling software was used to create a geometry of the geomechanical model with the horizons and faults as the input as well as the wells and the markers. As a note, the nomenclature of the horizons were changed from based on the base of formation/group into the top of formation/group. Since naming the horizons based on top of the horizons were more convenient for JewelSuite to work with.

The workflow of the geomechanical modeling using the JewelSuite comprehended some steps such as the stratigraphic modeling, fault modeling, 3D structural modeling and 3D mesh structural modeling. The stratigraphic and fault model were the input for the 3D structural model and 3D structural model was the input for 3D mesh structural model. This workflow was taken from the manual of this software (Taylor, Steehouwer, Turmaine, & van Ratingen, 2016).

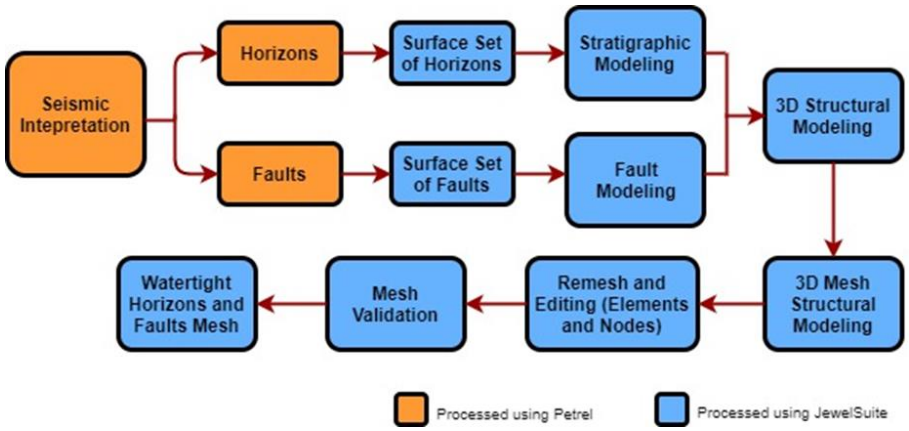

Figure 10. Workflow used to build 3D geological model.

Before entering the steps mentioned above, the horizons and faults imported to JewelSuite were classified into two separate surface sets, horizon surface set (containing horizons only) and fault surface set (containing faults only).

The stratigraphic modeling intended to contain and list the sequence and the order of the horizons in the model from the top of the model into the bottom of the model based on the markers or interpreted horizons. It was also used to define the zonation between each horizons and as the hierarchy where all the horizons were related each other. This step was needed to proceed to the next step where the actual horizons were assigned in the 3D structural model. In this case, the horizons in the horizons surface set were used as an input. The result of the stratigraphic model can be seen in the Figure 11.

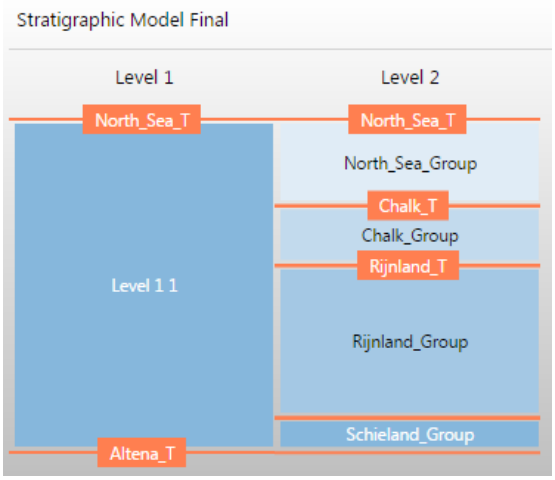

Figure 11. Stratigraphic model created in this model. From the top to the bottom of the model, the sequence of the horizons were following the interpreted horizons from seismic interpretation.

Fault modeling was an optional step for building the 3D structural model. But it was become a necessary step when the faults were taken into account to the model thus created more complex model. This step can be skipped if the faults were not included into the model. In this case, the faults were available so the fault modeling needed to be performed. The process of building the fault model was consisted of choosing the fault surface set as the input and solving the fault interactions because between two or more faults were not allowed to intercept each other. To ensure all the fault were not intersected each other, the faults were retracted (separation) and extended (filling the gap between the faults). An example of fault modeling in this model is depicted in Figure 12. Seven faults were associated within the model.

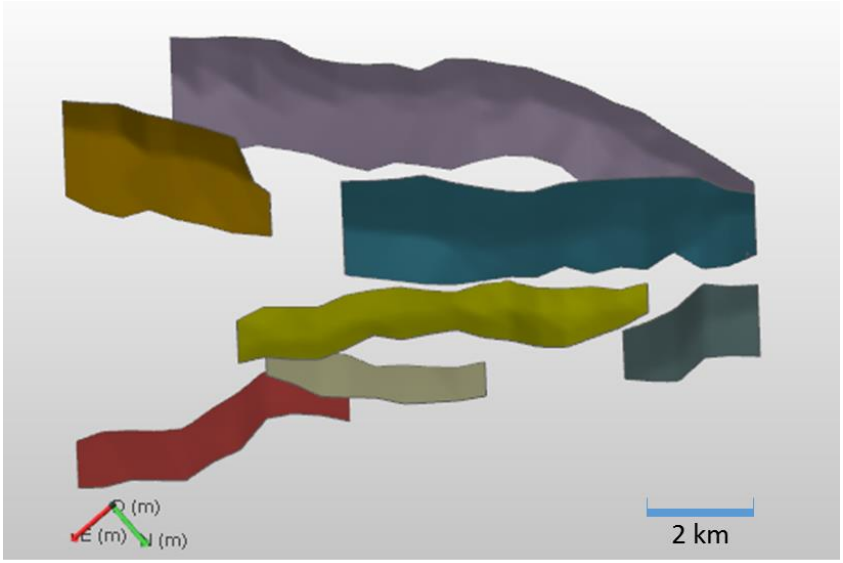

Figure 12. Fault modeling created in this model (top view). It can be observed, there are 7 faults involved in this model (depth scale ratio = 3).

3D structural model was the integration among the stratigraphic, fault model, horizons surface set and markers. During this process, the intersection between the horizons and the faults can be cleared using the horizon clean-up and fault cutoff lines options. The final output was the clean horizons and faults which had no intersection. The output of this process was used as the input for 3D mesh structural modeling. 3D structural model in this model can be seen in Figure 13 as an example.

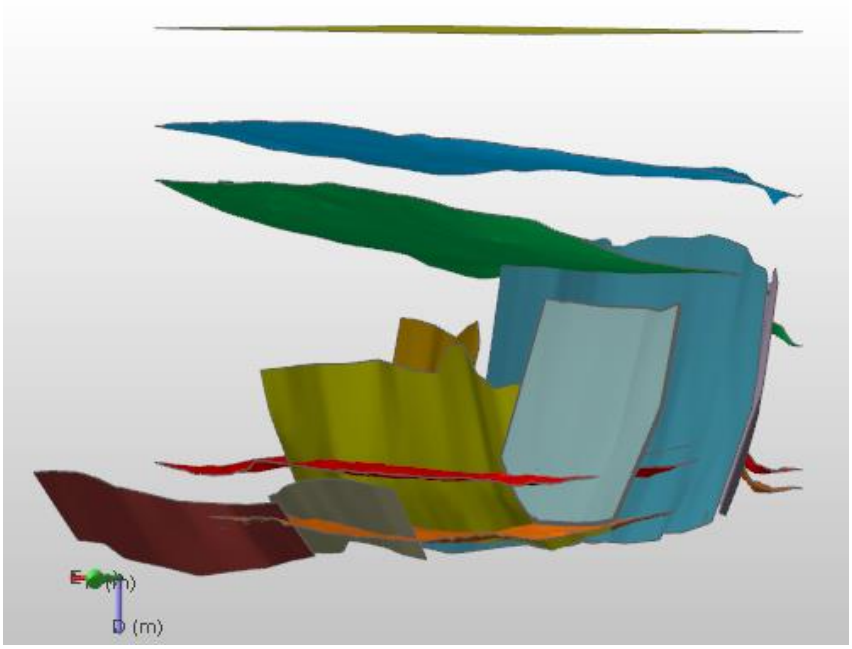

Figure 13. 3D structural model depicted the horizons and faults in the model.

JewelSuite 6.2 Subsurface Modeling is integrated with several add-ins including connector to Abaqus/CAE (Complete Abaqus Environment) software from Dassault Systèmes which is a software using to perform geomechanical simulation. In order to perform that simulation, 3D mesh structural modeling needed to be performed in JewelSuite because this 3D mesh structural model would be the input for simulation in Abaqus/CAE.

With 3D structural model in the previous step as an input, the main purpose of 3D mesh structural modeling process was to create the mesh of horizons and faults. The other function of 3D mesh structural modeling was to reduce the number of the elements and nodes thus creating a coarser mesh in each of the surfaces. The process of coarsening the mesh was conducted using “re-meshing” feature. Each surfaces had their own coarsening parameter.

Table 6 shows the number of elements and nodes before and after re-meshing. After re-meshing the number of elements decreases almost 8 times fewer than before re-meshing. Meanwhile, the total number of nodes (summation of the number of boundary nodes and nodes) decreases about 5 times fewer.

Number of -	**Before re-meshing**	**After-re-meshing**
Boundary nodes	3231	1949
Nodes	32450	5278
Elements	61645	8583

Table 6. Number of nodes and elements before and after re-meshing.

Although the re-meshing process would decrease the detail of the surfaces, re-meshing is important to reduce the computational work and decrease the amount of time used to run the simulation on the next step.

Furthermore, it is important to make sure that the contact between each the surfaces (horizons and faults) in this process is in watertight connection. This means that the surfaces not only did not have any intersection each other but also there are no gap between them. This watertight connection was the key point to the next step of modeling and simulation since if the watertight connection had not reached, all the modeling and simulation process would be error thus could not continue to the next steps.

The output of 3D mesh structural model was similar with 3D structural model in terms of appearance but 3D mesh structural model had coarser tri-mesh shape surfaces. After the 3D mesh structural modeling had been completed, those surfaces were ready to export to the Abaqus/CAE software.

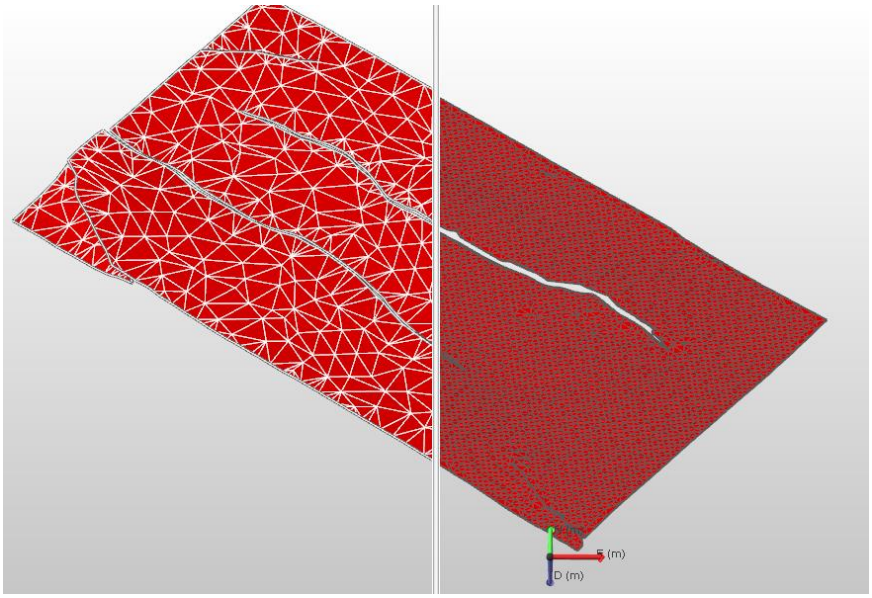

Figure 14. Comparison between 3D structural model (right) and 3D mesh structural model (left), example of Top Schieland horizon. Number of elements on the left picture reduced significantly from the right picture.

4.3. Finite Element Meshing

The integration between JewelSuite 6.2 Subsurface Modeling and Abaqus/CAE software from Dassault Systèmes was allowed the 3D meshing process in the Abaqus/CAE with 3D mesh structural model from JewelSuite as the input. The goal was solely to create 3D finite element mesh of the model. Unlike the previous step (3D mesh structural modeling) where it was only "mesh" the surfaces, the 3D mesh created using Abaqus/CAE would create full 3D mesh. Besides the 3D mesh structural model, a single well also needed in order to create 3D mesh.

To create the Finite Element Mesh in JewelSuite, the depth of the model and the area confined the model had to be specified and the surfaces from the 3D mesh structural model were selected. The size of the area meant here is 5.2 x 9.7 km, slightly smaller than the area of L3NAM1990C seismic sub-volume. The element type of each surfaces can be assigned here. There were several choice of element type provided by the Abaqus/CAE and JewelSuite as listed in the Table 7.

Element Type	**Explanation**
C3D10M	Continuum stress, 3D, 10-node elements, modified
C3D10MP	Continuum stress, 3D, 10-node elements, modified, pore pressure element
C3D10	Continuum stress, 3D, 10-node elements
C3D10P	Continuum stress, 3D, 10-node elements, pore pressure element

Table 7. Element type used in Abaqus/CAE and JewelSuite.

The selected well was the LIR-GT-01. There was no special reason for selecting this well since the mesh size in this study were uniform, 200 m. If non-uniform mesh size was desired, the selection of the well is important.

Several parameters related with the size of the mesh were needed to be adjusted. Such as the inner and outer radius, inner and outer mesh size and base layer size. The illustration of these radius and mesh size can be seen in Figure 15. The values of these parameters are listed on Table 8.

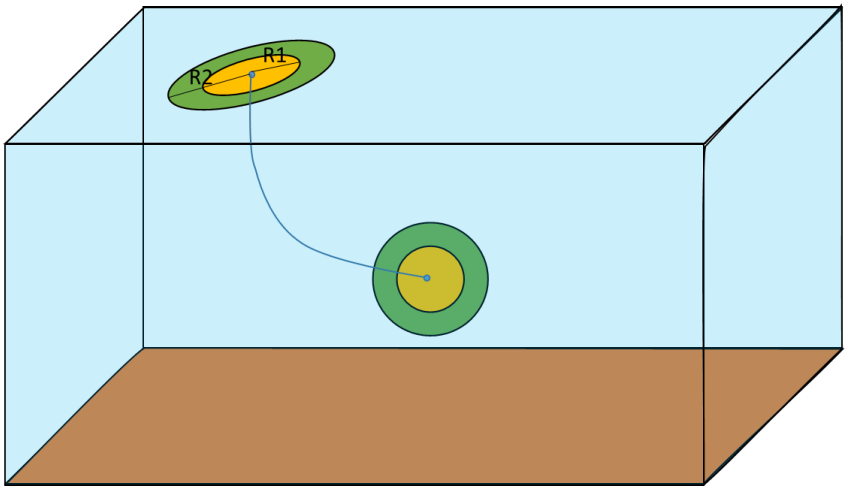

Figure 15. Illustration of mesh parameters. R1: inner radius, R2: outer radius, yellow: inner mesh size, blue: outer mesh size, blue: outer mesh size, green: interpolated between inner & outer mesh size, brown: base layer mesh size.

Parameter	**Value**
Inner radius	1000 m
Outer radius	2000 m
Inner mesh size	200 m
Outer mesh size	200 m
Base layer size	200 m

Table 8. Parameter value related with the 3D meshing.

Once all the parameter was filled with the values above in the JewelSuite software, the process of building the 3D finite element mesh was executed in the Abaqus/CAE. After the Abaqus/CAE finished running the meshing process, the output would be a full 3D mesh as depicted on the Figure 16.

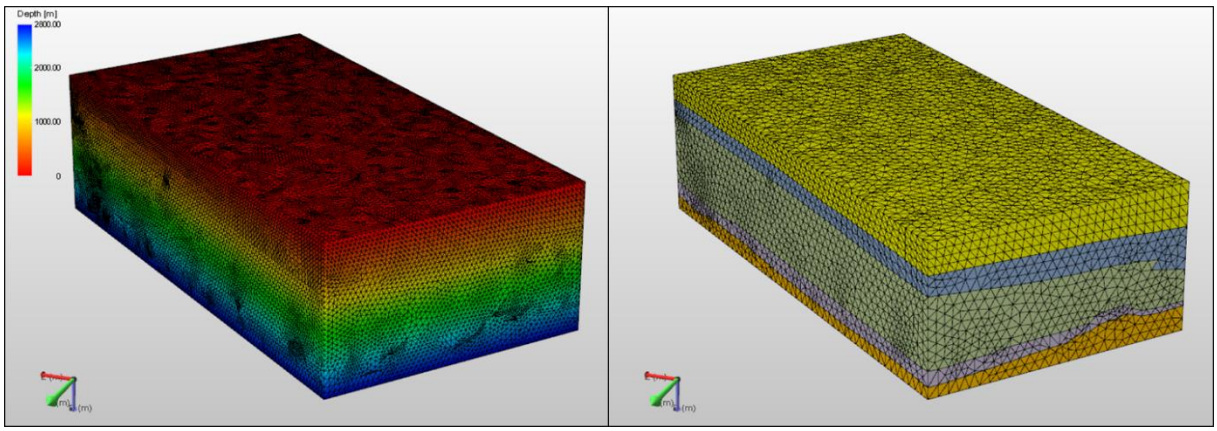

Figure 16. 3D finite element mesh generated by Abaqus/CAE. Viewed in JewelSuite. Left image: 3D FE-mesh with its corresponding depth. Right image: 3D FE-mesh with its corresponding formation/group (Gray: North Sea Group, Blue: Chalk Group, Green: Rijnland Group, Orange: Altena Group).

5. Geomechanical Simulation and Scenarios

The 3D finite element mesh was the base framework for all the simulation run in this study. This 3D model was ready to populate with the rock materials and simulated in order to generate stress distribution within the model. But before the geomechanical simulation started, there were some parameter needed to be adjusted such as rock properties and boundary condition.

5.1. Parameter Input

The rock and mechanical properties of each formation mostly were adjusted based on the NAM report as shown in Table 9 (Technical addendum to the Winningsplan Groningen 2013 subsidence, induced earthquakes and seismic hazard analysis in the Groningen Field, 2013). The rock and mechanical properties of Schieland and Altena Group were not covered in this report, but here they were assumed to have the same properties as the Rijnland and Triassic Group. This was because the Schieland and Altena Group were located between the Rijnland and Triassic in terms of depth and age (see Figure 3).

Stratigraphy Unit	**Density [kg/m2]**	**Young's Modulus [GPa]**	**Poisson's Ratio [-]**
North Sea Group	2150	2	0.3
Chalk Group	2350	10	0.25
Rijnland Group	2350	16	0.25
Schieland Group	2350	16	0.25
Altena Group	2350	16	0.25

Table 9. Elastic material properties and density used for each stratigraphic units.

In the 3D model, the other modified parameter was boundary conditions. The boundary condition was set into the fixed displacement at the bottom boundary. On the side boundary, the node-set cannot move along the horizontal direction but it can move in z-direction (depth direction). Thus the top boundary can move along the z-direction. The illustration of this boundary conditions can be found in Figure 17.

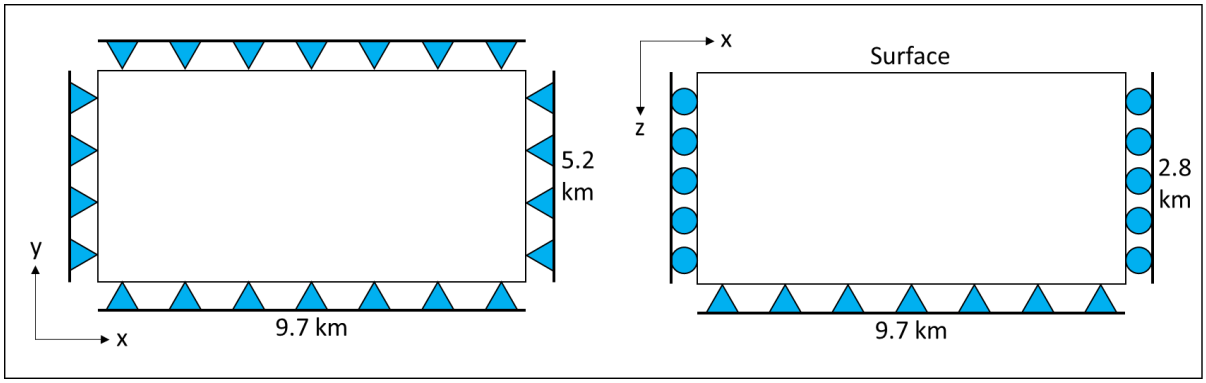

Figure 17. Illustration of boundary conditions of the model. x and y are the horizontal directions and z is depth direction. Left: top view of model, right: cross section view of the model.

5.2. Scenarios

The 3D geological model discussed in chapter 4 was successfully built. This model was populated with the rock properties in chapter 5.1. However, in order to running the geomechanical simulation, there was another parameter input which was the effective stress ratio. The equation used to calculate the ESR can be seen in chapter 2.2. Based on this formula, to calculate the ESR, the magnitude of tectonic stress had to be specified.

Several values of tectonic stress had been applied to running the geomechanical simulation. And each of these different magnitude of tectonic stresses became a different simulation scenario. Therefore, varying these tectonic stresses as the input of simulation was the simulation strategy in order to evaluate the stress regime and state of stress in this area.

5.2.1. Gravity-Only Scenario

The first scenario was the gravity-only scenario. In this case, the only source of the stress was the gravity which translated to overburden for both vertical and horizontal stress. The tectonic stress was absent in this scenario. In the other words, the tectonic stress was zero. The horizontal stresses were originated from the vertical stress and the magnitudes were controlled by the Poisson effect to all the horizontal directions (Bertotti, et al., 2017). Thus, the value of the horizontal stresses would be the same in all horizontal directions. On the other words, the maximum and minimum horizontal stress were equal in terms of magnitude.

In this case, the maximum principal stress was always be the vertical stress. Consequently, from the surface to the bottom of this model, the normal faulting regime was occurred.

The equation to calculate the vertical and horizontal stress can be found in chapter 2.2. It was simplified into the equation below with the pore pressure assumed to be zero for simplicity. Therefore, the effective stress would equal to the total stress itself. The equation of horizontal stress was simplified into the equation below,

$$S_h = \sigma_h = \frac{v}{1-v}\rho g z$$

This equation is similar with the equation purpose by Eaton, 1969. The list of Poisson's ratio at each stratigraphic unit can be found in Table 9.

5.2.2. Gravity-Tectonic Scenarios

As the name implied, the gravity-tectonic scenarios were the simulation where they were not only involving the gravity but also the tectonic stress. One of the source of the tectonic stress could be because of the tectonic plate movement. In this case, it was the movement of European and African plate. The gravity-tectonic scenarios were divided into 3 scenarios where the magnitude of the tectonic stress was varying, 10, 20, and 30 MPa.

Since the horizontal stresses in these scenarios were involving the tectonic stress, the maximum and minimum horizontal stress might be different. The maximum horizontal stress was the result of the tectonic stress and the Poisson's effect of the overburden. Meanwhile, the minimum horizontal stress was the result of the Poisson's effect of both overburden and tectonic stress. The equation to calculate horizontal stresses can be found in chapter 2.2. The assumption for the magnitude of pore pressure was the same as in gravity-only scenario where the pore pressure was assumed to be zero for simplicity. The equation for minimum and maximum horizontal stress was simplified into the equation below,

$$S_{hmin} = \sigma_{hmin} = \left(\frac{v}{1-v}(\rho g z)\right) + \left(\frac{v}{1-v}(S_{tect})\right)$$

$$S_{Hmax} = \sigma_{Hmax} = \left(\frac{v}{1-v}(\rho g z)\right) + S_{tect}$$

In these scenarios, the horizontal stresses were always present from the surface to the bottom of the model. At the deeper depth, the influence of the gravity (vertical stress) was increasing. On the other hand, at shallower depth, the horizontal stresses had a bigger role. Even though, at the near surface depth, the unconsolidated formation might present and dissipated the stress (Zoback M. D., Reservoir Geomechanics, 2007), it was not necessarily always the case. Based on the stress measurement in some experiments in several places in the world (Brown & Hoek, 1978), the stress ratio in the near surface was not nearly zero. In fact, a lot of data points had values more than 1 indicating that the horizontal stress played bigger role in the near surface than the vertical stress. This assumption was used in these scenarios as the input of stress ratio.

The summary of the simulation scenarios can be found in table below,

Scenario	**Source of stress**	**Tectonic stress [MPa]**
Scenario 1	Gravity-only	0
Scenario 2	Gravity-tectonic	10
Scenario 3	Gravity-tectonic	20
Scenario 4	Gravity-tectonic	30

Table 10. Summary of simulation scenario.

5.3. Results and Discussion

The scenarios discussed above were simulated in 3D geological model using the Abaqus/CAE software. But before the 3D simulation was conducted, the 1D stress model was built. 1D stress model basically is considered as a layer cake geological model which has a constant depth for every stratigraphic units throughout the entire area.

5.3.1. 1D Stress Model

The input for 1D stress model was effective stress ratio and its corresponding depth. The parameter to calculate the stress ratio was listed on the Table 9. The complete calculation can be found in the figure below.

Unit	Depth (m)	Density	Poisson's Ratio	Sv (MPa)	Scenario 1 Shmin (tect = 0)	Scenario 2 Shmin (tect = 10)	Scenario 3 Shmin (tect = 20)	Scenario 4 Shmin (tect = 30)	Scenario 1 SHmax (tect = 0)	Scenario 2 SHmax (tect = 10)	Scenario 3 SHmax (tect = 20)	Scenario 4 SHmax (tect = 30)
North Sea	0	2150	0.3	0	0.000	4.286	8.571	12.857	0.000	10.000	20.000	30.000
North Sea	200	2150	0.3	4.2183	1.808	6.094	10.379	14.665	1.808	11.808	21.808	31.808
North Sea	400	2150	0.3	8.4366	3.616	7.901	12.187	16.473	3.616	13.616	23.616	33.616
North Sea	600	2150	0.3	12.6549	5.424	9.709	13.995	18.281	5.424	15.424	25.424	35.424
Chalk	800	2350	0.25	17.2656	5.755	9.089	12.422	15.755	5.755	15.755	25.755	35.755
Chalk	1000	2350	0.25	21.8763	7.292	10.625	13.959	17.292	7.292	17.292	27.292	37.292
Chalk	1200	2350	0.25	26.487	8.829	12.162	15.496	18.829	8.829	18.829	28.829	38.829
Rijnland	1400	2350	0.25	31.0977	10.366	13.699	17.033	20.366	10.366	20.366	30.366	40.366
Rijnland	1600	2350	0.25	35.7084	11.903	15.236	18.569	21.903	11.903	21.903	31.903	41.903
Rijnland	1800	2350	0.25	40.3191	13.440	16.773	20.106	23.440	13.440	23.440	33.440	43.440
Rijnland	2000	2350	0.25	44.9298	14.977	18.310	21.643	24.977	14.977	24.977	34.977	44.977
Schieland	2200	2350	0.25	49.5405	16.514	19.847	23.180	26.514	16.514	26.514	36.514	46.514
Schieland	2400	2350	0.25	54.1512	18.050	21.384	24.717	28.050	18.050	28.050	38.050	48.050
Schieland	2600	2350	0.25	58.7619	19.587	22.921	26.254	29.587	19.587	29.587	39.587	49.587
Altena	2800	2350	0.25	63.3726	21.124	24.458	27.791	31.124	21.124	31.124	41.124	51.124

Unit	Depth (m)	Scenario 1 σhmin/Sv (tect = 0)	Scenario 2 σhmin/Sv (tect = 10)	Scenario 3 σhmin/Sv (tect = 20)	Scenario 4 σhmin/Sv (tect = 30)	Scenario 1 σhmax/Sv (tect = 0)	Scenario 2 σhmax/Sv (tect = 10)	Scenario 3 σhmax/Sv (tect = 20)	Scenario 4 σhmax/Sv (tect = 30)
North Sea	0	0.429	2.211	4.166	6.120	0.429	5.057	9.857	14.657
North Sea	200	0.429	1.445	2.461	3.477	0.429	2.799	5.170	7.540
North Sea	400	0.429	0.937	1.445	1.953	0.429	1.614	2.799	3.985
North Sea	600	0.429	0.767	1.106	1.445	0.429	1.219	2.009	2.799
Chalk	800	0.333	0.526	0.719	0.913	0.333	0.913	1.492	2.071
Chalk	1000	0.333	0.486	0.638	0.790	0.333	0.790	1.248	1.705
Chalk	1200	0.333	0.459	0.585	0.711	0.333	0.711	1.088	1.466
Rijnland	1400	0.333	0.441	0.548	0.655	0.333	0.655	0.976	1.298
Rijnland	1600	0.333	0.427	0.520	0.613	0.333	0.613	0.893	1.173
Rijnland	1800	0.333	0.416	0.499	0.581	0.333	0.581	0.829	1.077
Rijnland	2000	0.333	0.408	0.482	0.556	0.333	0.556	0.778	1.001
Schieland	2200	0.333	0.401	0.468	0.535	0.333	0.535	0.737	0.939
Schieland	2400	0.333	0.395	0.456	0.518	0.333	0.518	0.703	0.887
Schieland	2600	0.333	0.390	0.447	0.504	0.333	0.504	0.674	0.844
Altena	2800	0.333	0.386	0.439	0.491	0.333	0.491	0.649	0.807

Figure 18. Complete calculation of effective stress ratio used in all the simulation scenarios.

After that, both effective stress ratio (ESR) for minimum and maximum horizontal stress were plotted against depth as depicted in Figure 19.

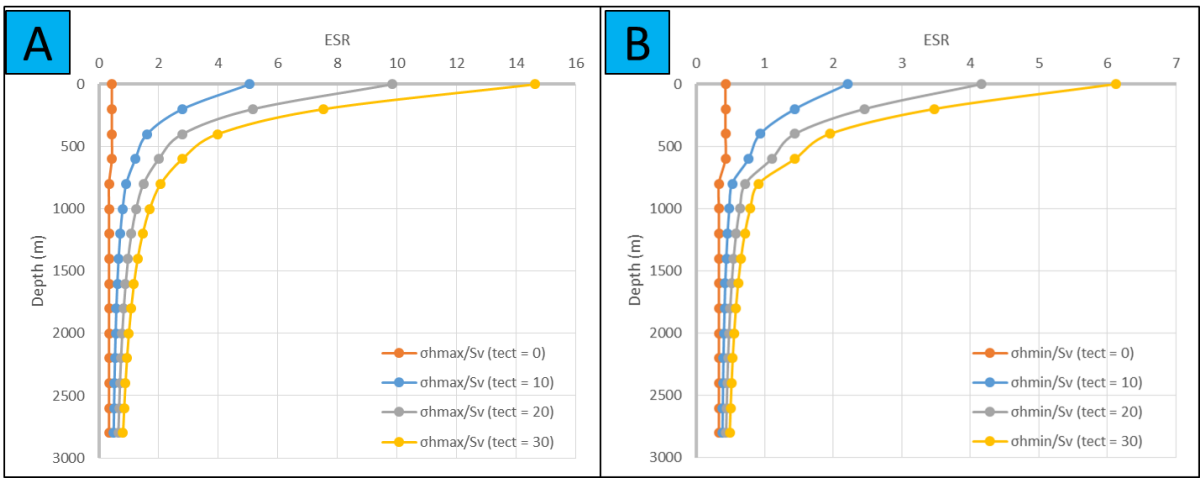

Figure 19. Effective stress ratio for maximum horizontal stress (A) and minimum horizontal stress (B).

The effective stress ratio was plotted for all scenarios. It can be seen from both graphs above, as the tectonic stress is increasing, the effective stress ratio is also increasing. This is due to the increasing of magnitude of maximum and minimum horizontal stress. Moreover, the ESR at the shallower depth is higher than the ESR at the deeper depth. It is because at the shallower depth, the horizontal stress has a bigger role than the vertical stress.

5.3.1.1. Scenario 1: Gravity-Only Scenario

As it was explained in chapter 5.2.1, the only source of the stresses was the gravity. From Figure 20, it can be seen that the minimum and maximum horizontal stress are equal. From the top until the bottom of the model, the vertical stress is always bigger than the horizontal. This is implying that there is only one stress faulting regime, normal faulting regime.

Since the density of each stratigraphic units is similar (Table 9), the difference in the slope of the vertical stress is not really visible. However, the difference in the slope of the horizontal stresses are clearly visible. It can be notice in the transition from the North Sea Group to the Chalk Group. This is due to the difference in Poisson's ratio of these stratigraphic units. Meanwhile, the slope of the horizontal stresses are the same from the Chalk Group to the bottom of the model since they have the same Poisson's ratios.

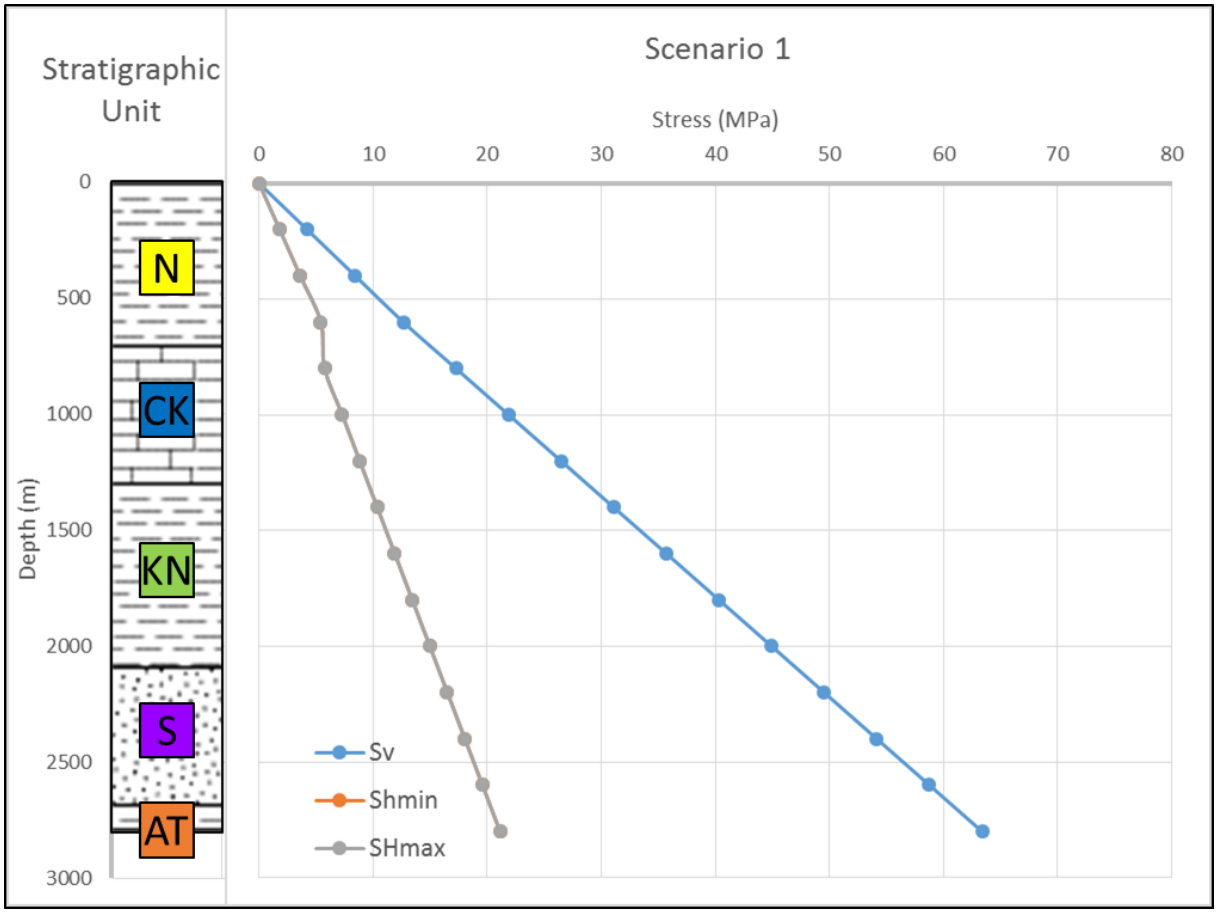

Figure 20. Pressure-depth curve for scenario 1 (gravity-only scenario). N: North Sea Group, CK: Chalk Group, KN: Rijnland Group, S: Schieland Group, AT: Altena Group.

5.3.1.2. Scenario 2: Gravity-Tectonic Scenario (Tect. Stress = 10 MPa)

The tectonic stress was included in the gravity-tectonic scenario in addition to gravity as source of stress. In this scenario, the tectonic stress had a magnitude of 10 MPa.

As it is seen in Figure 21, from the top to bottom of the model, the vertical stress is not always become the maximum principal stress in this scenario. Unlike the first scenario, the maximum, intermediate, and minimum principal stress are changing their direction through depth. From the surface until around 750 m, the maximum principal stress is the maximum horizontal stress. Meanwhile, below that depth, the maximum principal stress is the vertical stress.

From the Figure 21, there are 3 faulting regime from the top to the bottom of the model. The reverse faulting regime is observed from the top of the model until depth around 350 m. Then, the strike-slip faulting regime is occurred in depth between around 350 m until 750 m. From 750 m until the bottom of the model, normal faulting regime is followed.

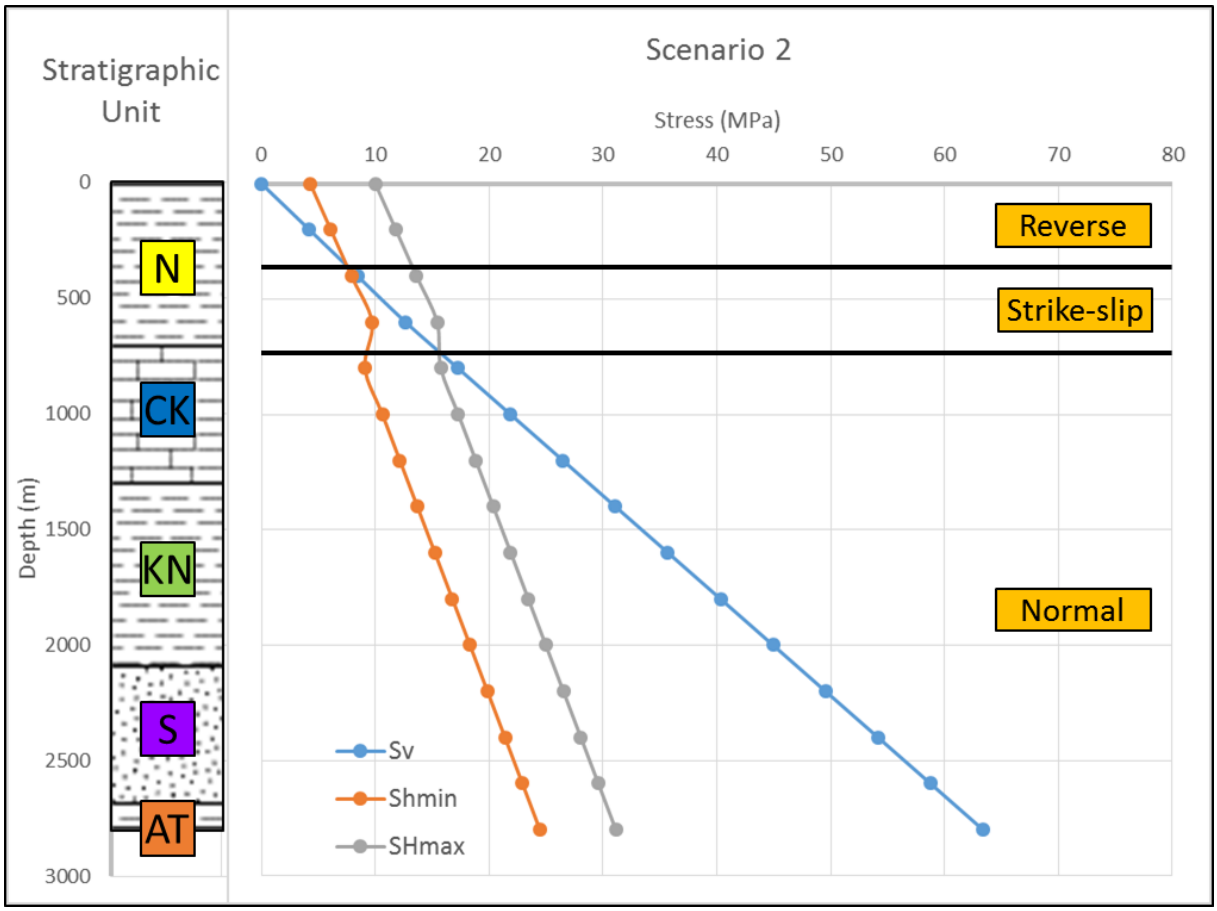

Figure 21. Pressure-depth curve for scenario 2 (gravity-tectonic scenario with tectonic stress 10 MPa). N: North Sea Group, CK: Chalk Group, KN: Rijnland Group, S: Schieland Group, AT: Altena Group.

5.3.1.3. Scenario 3: Gravity-Tectonic Scenario (Tect. Stress = 20 MPa)

The third scenario was similar with the second scenario where the tectonic stress was also included. The magnitude of the tectonic stress was 20 MPa for this scenario. All principal stresses orientation is changing through the depth as it can be seen in Figure 22. The maximum principal stress direction is at the maximum horizontal stress direction from depth 0 until around 650 m and at the rest of the remaining depth is on the vertical stress direction.

As it is shown in Figure 22, there are 3 stress faulting regimes observed in this scenario, reverse faulting regime at the shallower part of the model and normal faulting regime in the deeper part of the model and between them, strike-slip faulting is observed from depth around 650 m and 1350 m.

Comparing the result of this scenario and the scenario 2, the thickness of each faulting regime zone is thicker here. In this scenario, the thickness of reverse and strike-slip faulting regime is reaching around 650 m and 750 m, respectively. Meanwhile, in the previous scenario, these thicknesses are just around 350 m and 400 m for reverse and strike-slip faulting, respectively.

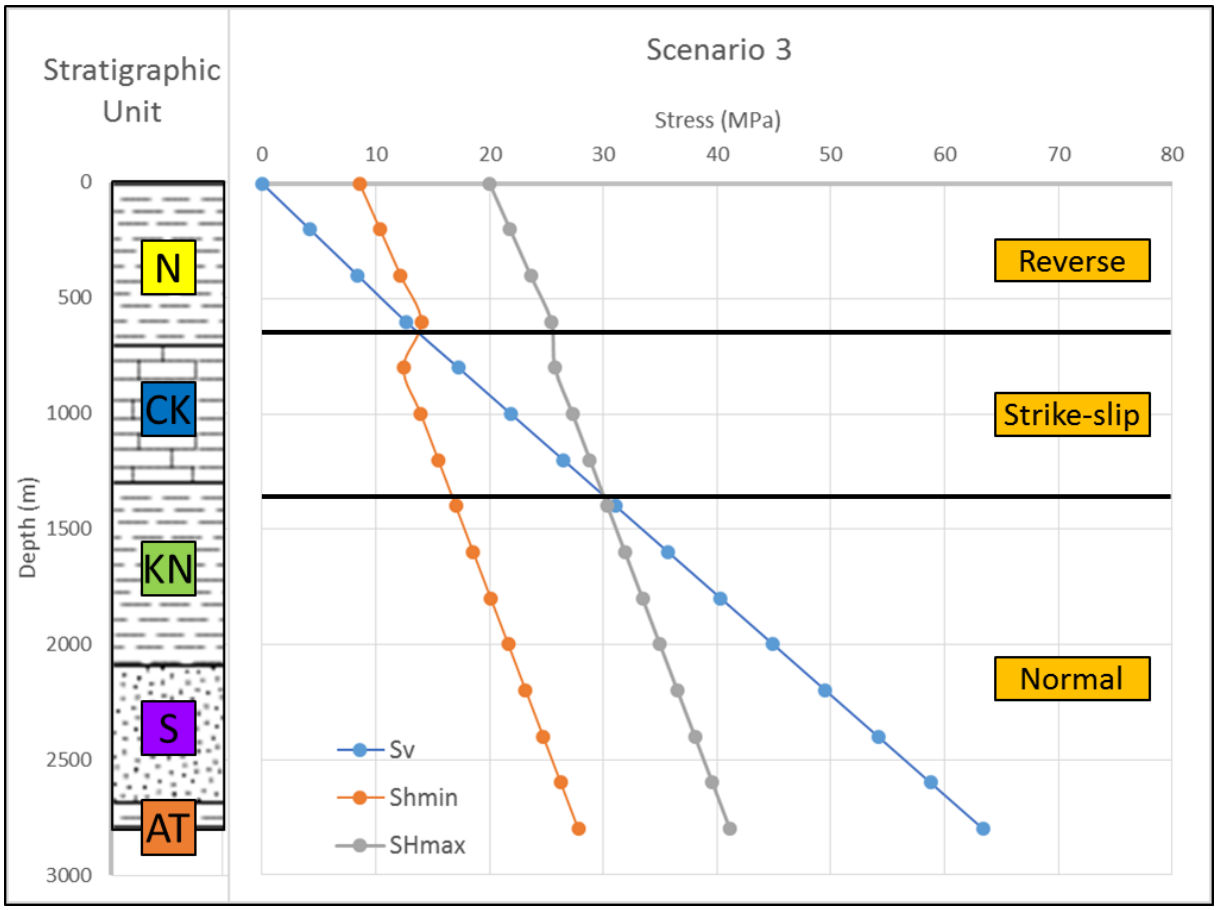

Figure 22. Pressure-depth curve for scenario 3 (gravity-tectonic scenario with tectonic stress 20 MPa). N: North Sea Group, CK: Chalk Group, KN: Rijnland Group, S: Schieland Group, AT: Altena Group.

5.3.1.4. Scenario 4: Gravity-Tectonic Scenario (Tect. Stress = 30 MPa)

The last scenario was also similar with the two previous scenarios where the tectonic stress was included as the source of stress. 30 MPa was the magnitude of tectonic stress using in this scenario.

Based on Figure 23, the maximum horizontal stress still becomes the maximum principal stress at least until it reaches depth 2000 m. Three faulting regimes are also be found in this scenario. The reverse faulting regime is occurred from the top of the model until the depth around 750 m. The strike-slip faulting regime is happened between depth 750 m and 2800 m while the remaining depth is normal faulting regime.

Moreover, the thickness of each faulting regime zone on this scenario is even greater than the previous two scenarios. The thickness of reverse faulting regime zone is 750 m and strike-slip faulting regime zone is 1250 m.

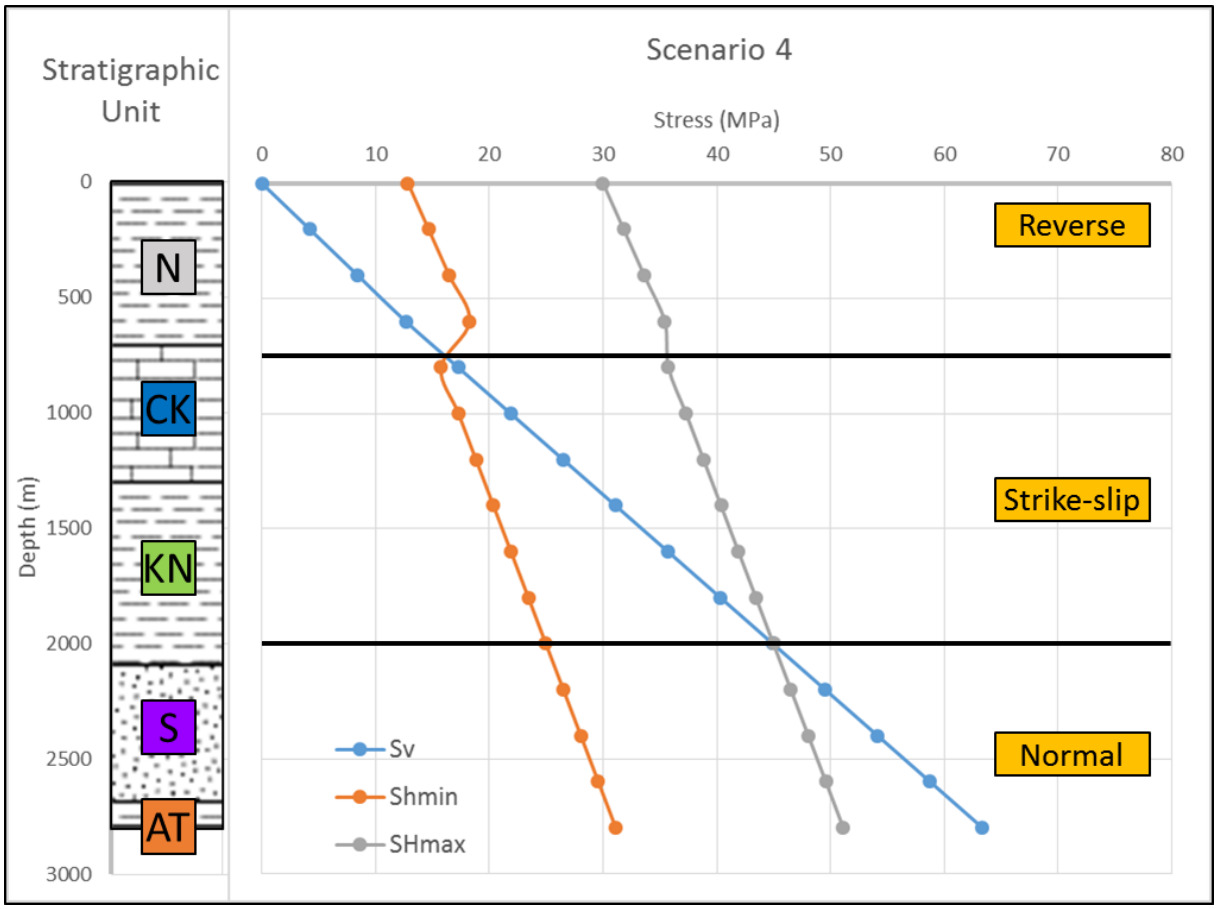

Figure 23. Pressure-depth curve for scenario 4 (gravity-tectonic scenario with tectonic stress 30 MPa). N: North Sea Group, CK: Chalk Group, KN: Rijnland Group, S: Schieland Group, AT: Altena Group.

5.3.1.5. Comparison of Scenario Results

Table 11 is providing the summary of stress faulting regimes with their corresponding depth for each scenarios.

Scenario	Stress regime	Depth (m)	σ1	σ2	σ3
Scenario 1	Normal faulting	0 - 2800	Sv	SHmax	Shmin
Scenario 2	Reverse faulting	0 - 350	SHmax	Shmin	Sv
	Strike-slip faulting	350 - 750	SHmax	Sv	Shmin
	Normal faulting	750 - 2800	Sv	SHmax	Shmin
Scenario 3	Reverse faulting	0 - 650	SHmax	Shmin	Sv
	Strike-slip faulting	650 - 1350	SHmax	Sv	Shmin
	Normal faulting	1350 - 2800	Sv	Shmin	Shmin
Scenario 4	Reverse faulting	0 - 750	SHmax	Shmin	Sv
	Strike-slip faulting	750 - 2000	SHmax	Sv	Shmin
	Normal faulting	2000 - 2800	Sv	SHmax	Shmin

Table 11. Summary of stress faulting regimes with the principal stresses orientation for all scenarios.

It can be concluded that in the scenario where the tectonic stress is not included, there is only one stress regime observed, normal faulting regime. On the other hand, in the scenarios where the tectonic stress is involved, there are three stress regimes observed, reverse, strike-slip, and normal faulting regime. However, these stress regimes are occurred in the different depth between the scenarios. As the tectonic stress is higher, the thickness of the zone where the reverse and strike-slip stress regime occurred is increasing.

For the principal stresses orientation, in gravity-only scenario, the orientation is constant from surface to the bottom of model. On the other hand, the principal stresses orientations are changing throughout the depth in the gravity-tectonic scenarios.

5.3.2. 3D Stress Model

The 3D stress simulation was also using the same input as in 1D model. In the 3D stress model, the azimuth of the maximum horizontal stress (S_{Hmax}), N145ºE, was also used as an input. But the main difference was that in the 3D stress simulation, these input data were applied to the 3D geological model which in the previous chapter had been generated and assigned by different material properties on each stratigraphic units.

The ESR was also used and applied to the model with the same scenarios mentioned above. The result of the simulation was the 3D principal stresses distribution. For clear visualization and simplicity, there were several analyses conducted to visualize the 3D stress distribution. The analyses was involving the point analysis and cross section analysis.

Figure 24 is the example of cross section approximately in the middle of the model (see cross section 2 in Figure 26) with the intermediate principal stress (σ_2) distribution from scenario 3. The S_2 distribution is selected since based on the 1D stress analysis, the direction of σ_2 from surface to the bottom of the model is varied to the direction of S_{hmin}, S_{Hmax}, and S_v as it is shown in Figure 24.

The x, y, and z axis in this figure represent the east, north, and negative depth, respectively. The cross section is oriented NE-SW from left to right figure. In the shallower depth, around 0 – 700 m, the orientation of the σ_2 is mostly NE-SW which coincides with the orientation of S_{hmin}. At depth around 700 – 1500 m, the S_2 is mostly vertical which matches with the direction of S_v. Below the 1500 m, σ_2 is oriented to NW-SE, more or less the same as the azimuth of S_{Hmax}.

The variation of the principal stress orientation along the depth is also can be found in 1D model. But as it is seen in this figure, on the transition from one to another σ_2 orientation zone,

there are some perturbations in σ_2 orientation as it is shown at depth around 700 m in the transition from the S_{hmin} to S_v direction and at depth around 1400 m in the transition from the S_v to S_{hmin} direction. So in this transition zone, the principal stresses are not fit perfectly with the S_{hmin} to S_v orientation but oblique to them.

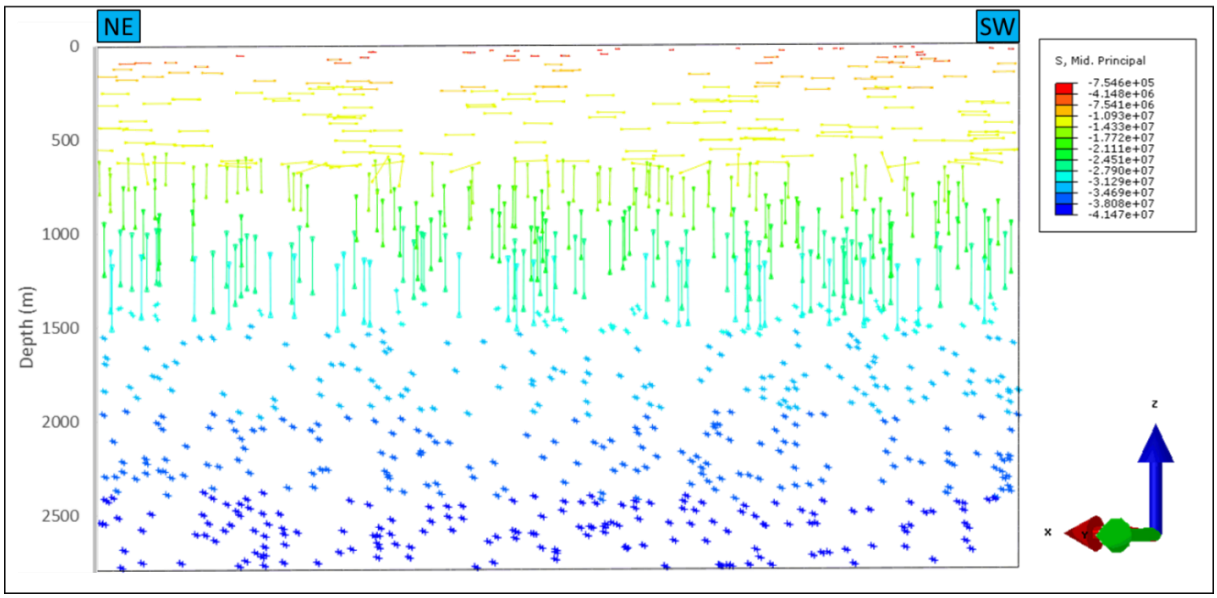

Figure 24. Example of cross section in NE-SW orientation with intermediate principal stress distribution. Color bar indicates the stress magnitude.

5.3.2.1. Point Analysis

The point analysis was performed as a preliminary analysis for the cross section analysis. This analysis was conducted in order to have an insight about the principal stress magnitude and orientation in the model using the 3D simulation. It is containing two points in the model at the same cross section as shown in Figure 24. The location of the cross section can be found in Figure 26. The goal is to analyse the principal stress magnitude and orientation of those points. The detail descriptions of those points are listed below.

Description	**Point A**	**Point B**
Element number	47035	74894
Node number	14832	19781
x-coordinate	6083.29	5012.36
y-coordinate	5373.12	3996.88
Depth	1744.29 m	1581.47 m

Table 12. Point A and B used as point analysis in 3D stress simulation.

The magnitude of principal stresses within point A and B can be seen in the Figure 25. It is provided the principal stresses for all the scenarios. The negative signs mean that they are in the compressive stress (engineering convention of Abaqus/CAE).

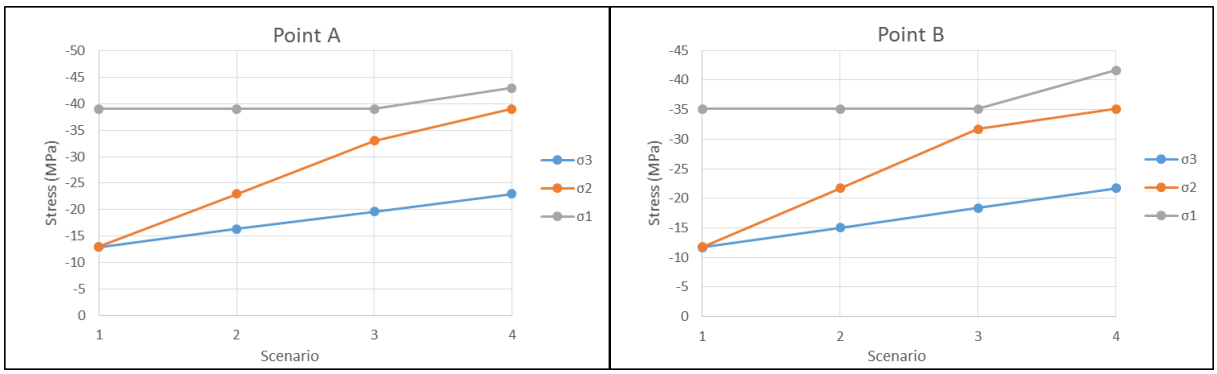

Figure 25. Magnitude of principal stresses in point A and B with different scenarios.

The point A and B located in depth 1744.29 m and 1581.47 m, respectively. From the figure above, the trend of the principal stress magnitude of those points are similar. In the scenario 1, the σ_2 and σ_3 magnitude are equal. Because the horizontal stresses in the gravity-only scenario (scenario 1) are also equal, the σ_2 and σ_3 in this scenario are translated as horizontal stresses.

The vertical stresses have the same magnitudes throughout the scenarios but not with the horizontal stresses. The σ_1 in the scenario 1, 2, and 3 have the same magnitudes. Therefore, in scenario 1, 2, and 3, the σ_1 is interpreted as the vertical stress.

The magnitude of σ_2 in the scenario 4 is the same as the magnitude of σ_1 in scenario 1, 2, and 3.This implies that in the scenario 4, the σ_2 is directed to the vertical direction since it is known that the magnitude of vertical stress is unchanged throughout scenarios.

It also shows that scenario 4 has a different stress regime than the other scenarios in the point A and B. The normal stress regime is observed in the scenario 1, 2, and 3. On the other hand, the strike-slip stress regime is observed in the scenario 4. The summary of the principal stresses orientation and stress regimes in the point A and B can be found in Table 13.

Scenario	**σ_1**	**σ_2**	**σ_3**	**Stress regime**
Scenario 1	S_v	S_{Hmax}	S_{hmin}	Normal faulting
Scenario 2	S_v	S_{Hmax}	S_{hmin}	Normal faulting
Scenario 3	S_v	S_{Hmax}	S_{hmin}	Normal faulting
Scenario 4	S_{Hmax}	S_v	S_{hmin}	Reverse faulting

Table 13. Direction of principal stresses and stress regimes for point A and B in all scenarios.

5.3.2.2. Cross Section Analysis

The cross section analysis was performed in order to analyse the principal stresses within the model especially to understand the stress distribution in lateral direction. Beside the principal stresses, the stress from an arbitrary direction in the model was also analysed.

The stresses are analysed throughout 4 cross sections that can be found in Figure 26. In each cross sections, the stresses are examined in two depths, 200 m and 2400 m depth for all 4 different scenarios. As a reminder, the scenario 1 is the gravity-only scenario. And the scenario 2, 3, and 4 are the gravity-tectonic scenarios with different magnitude of tectonic stress, 10, 20, and 30 MPa, respectively.

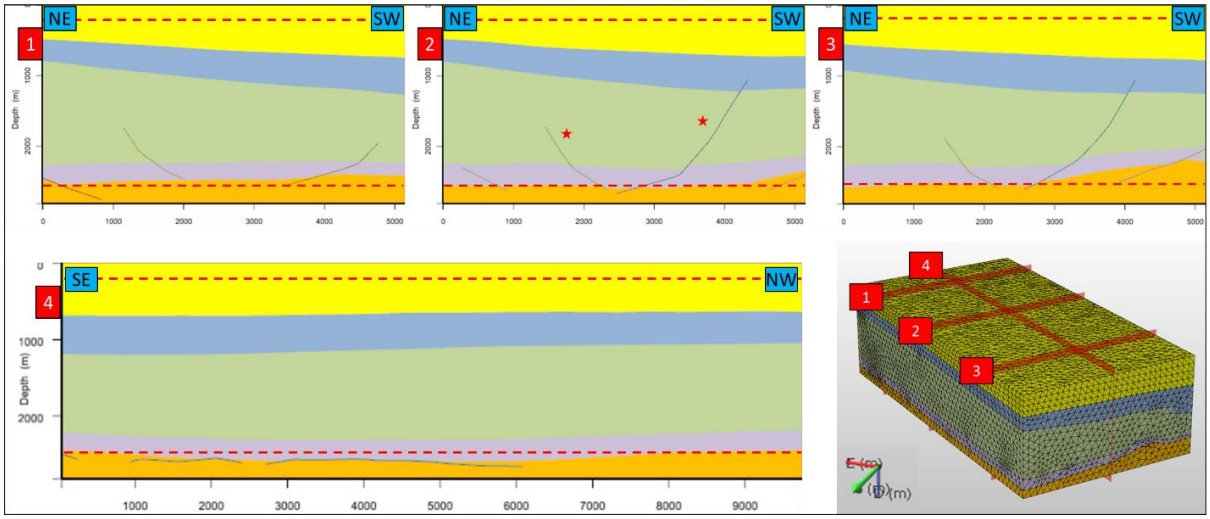

Figure 26. Four cross sections with their location in the model. The red-dashed lines indicate the locations of cross section analysis and red stars indicate the location of point analysis.

The principal stresses examined in the cross section 2 can be found in the Figure 27 and Figure 28 for depth 200 m and 2400 m, respectively. The negative signs of these principal stresses represent the compressive stress.

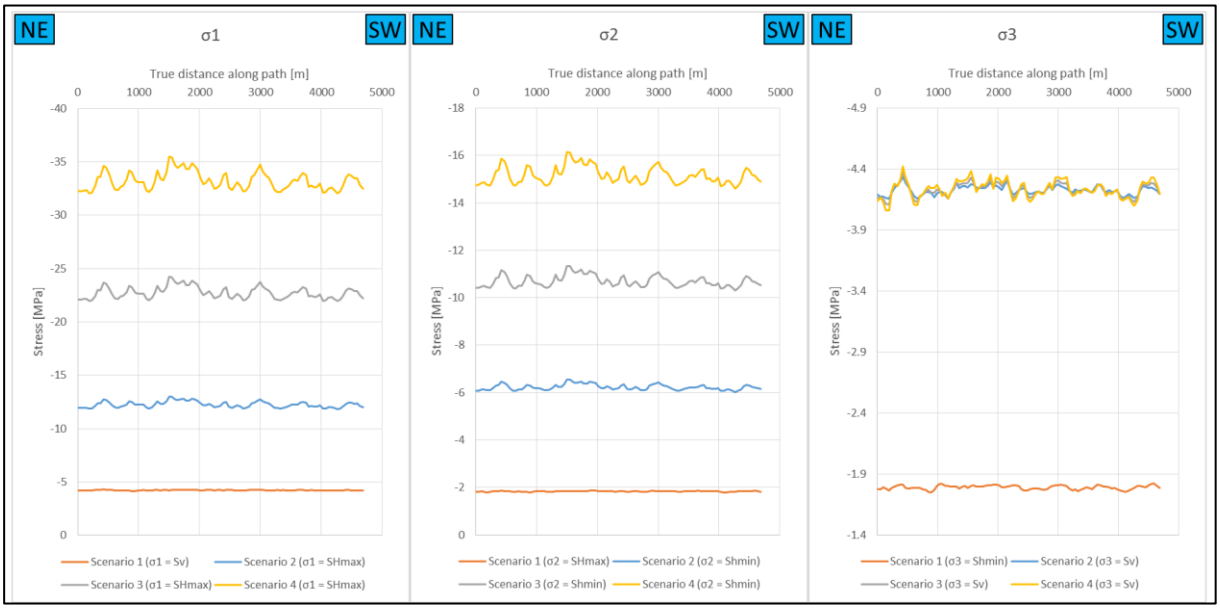

Figure 27. Magnitude of principal stresses in the cross section 2 at depth 200 m for different scenario. Left: maximum principal stress, middle: intermediate principal stress, right: minimum principal stress.

The magnitudes of all principal stresses fluctuate along the same depth as it is shown in Figure 27. In the all scenarios (gravity-only and gravity-tectonic scenarios), the relation between the magnitude of the principal stresses and the magnitude of the tectonic stresses are observed

here. As the tectonic stress becomes larger, the magnitude of all principal stresses is also larger. For instance, the magnitude of principal stresses in the scenario 4 is larger than the one in scenario 2. This relation of between tectonic stress and principal stress is valid to all principal stresses except the σ_3. The magnitudes of σ_3 in the gravity-tectonic scenarios are similar as it is shown in the right graph of Figure 27. This is due to the σ_3 in the gravity-tectonic scenario is vertical stress and the vertical stress is not affected by the tectonic stress.

It also can be pointed out that the magnitude of σ_2 and σ_3 in the gravity-only scenario has similar value implying that these principal stresses are the horizontal stresses since in the gravity-only scenario, the magnitude of maximum and minimum horizontal stress are equal.

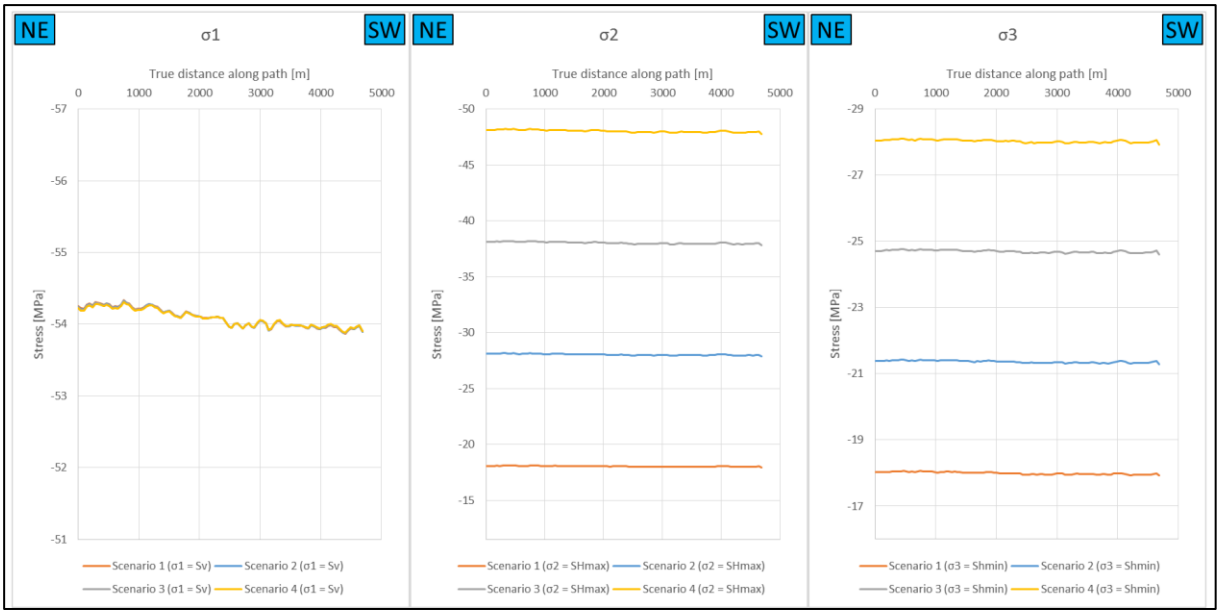

Figure 28. Magnitude of principal stresses in the cross section 2 at depth 2400 m for different scenario. Left: maximum principal stress, middle: intermediate principal stress, right: minimum principal stress.

Similar with the previous figure, in the Figure 28, the magnitudes of all principal stresses fluctuate along the same depth, 2400 m. One of the most noticeable feature in this figure is that the magnitudes of the σ_1 for all scenarios are almost identical. This is because at depth 2400 m, the σ_1 is the vertical stress and this vertical stress is only influenced by the overburden but not tectonic stress. Meanwhile, the relation between the magnitude tectonic stress and the other two principal stresses is just like at the depth 200 m. If the tectonic stress magnitude is large then the magnitudes of σ_2 and σ_3 are also large. As depicted in Figure 28, where the σ_2 and σ_3 in the scenario 4 is greater than in the scenario 1, 2, and 3.

It also can be noticed that the magnitude of σ_2 and σ_3 in the scenario 1 (gravity-only scenario) are alike indicating that these principal stresses are the horizontal stresses. Because in the gravity-only scenario, the magnitude of maximum and minimum horizontal stress are equal.

Beside the principal stresses, the magnitude of the stress in any arbitrary direction in the model also can be extracted. For instance, since the length of this geomechanical model is oriented to N128^{o}E, it is interesting to know the stress magnitude to this direction. In other words, it is good to know the magnitude of stresses that perpendicular and parallel to the plane of the model.

The positive x-axis direction in this new coordinate system is parallel to the length of the model and oriented to NW direction. The positive y-axis direction is perpendicular to the length of the model and oriented to SW direction. Meanwhile, the z-axis is vertical to the bottom of the model. The stress parallel to the x-axis, normal to the x-plane (width of the model) is called σ_x. The stress oriented to the y-axis, normal to the y-plane (length of the model) is called σ_y. And the stress normal to the surface is σ_z.

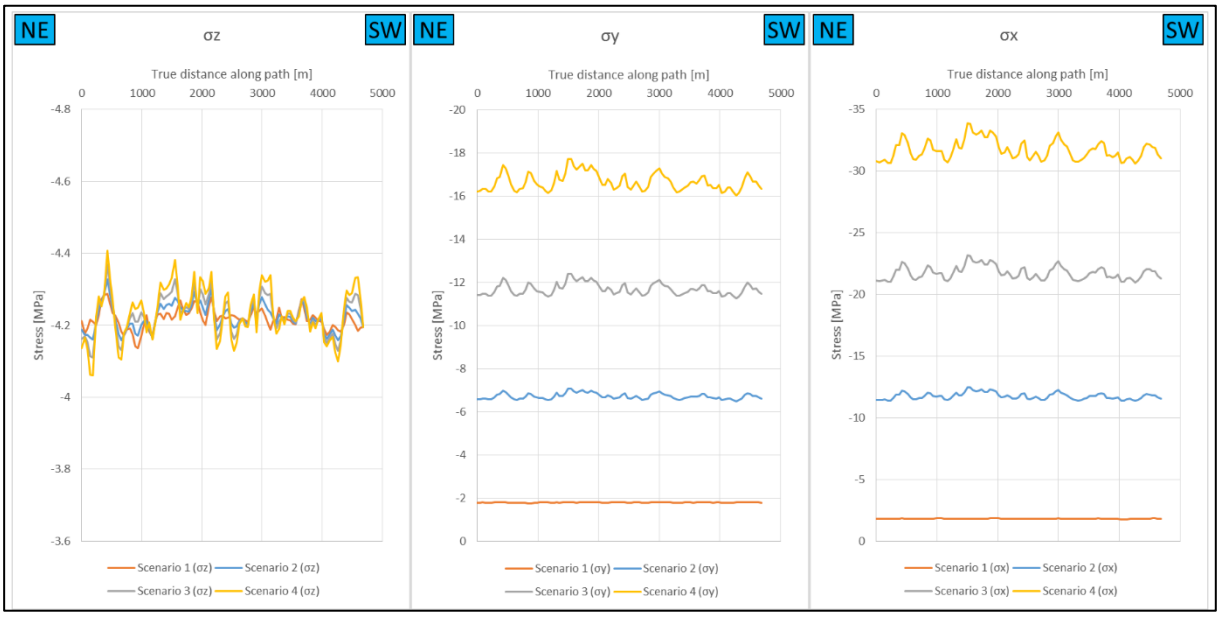

Figure 29. Magnitude of resulting stresses in the cross section 2 at depth 200 m for different scenario based on their directions.

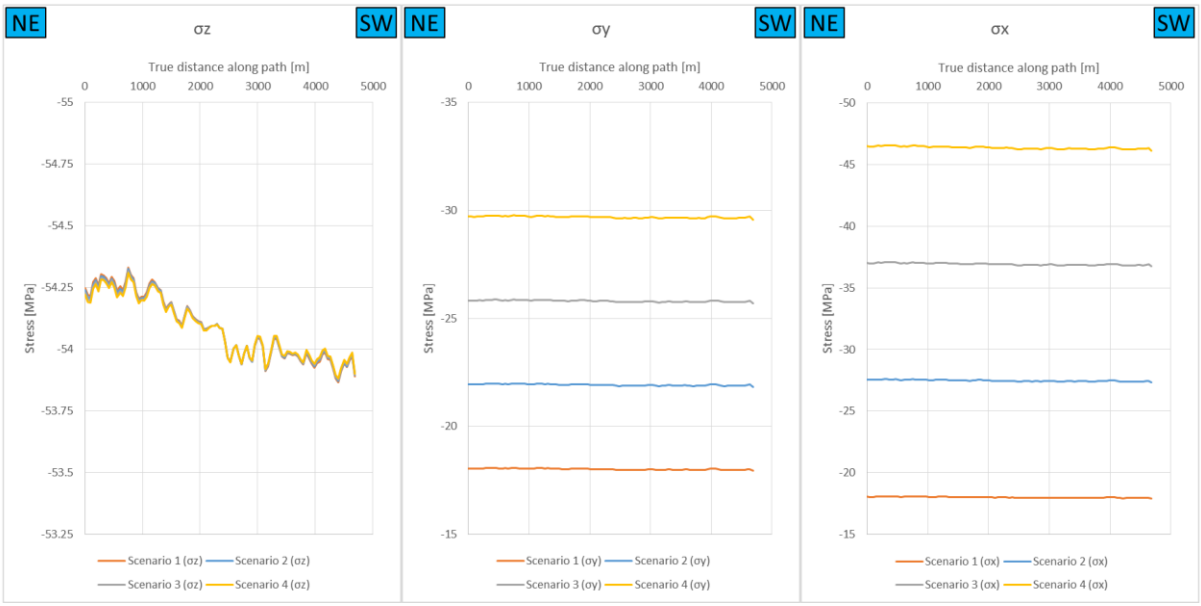

Figure 30. Magnitude of resulting stresses in the cross section 2 at depth 2400 m for different scenario based on their directions.

Figure 29 and Figure 30 illustrate the magnitude of these stresses at the cross section 2 (see Figure 26) at depth 200 m and 2400 m, respectively. The stress magnitudes in the Figure 29 shows the similar result with the one in the Figure 27 in the relation between the tectonic stress input and the resulting stress. Such as the σ_x and σ_y magnitude are increasing with the increasing of the tectonic stress. But the main difference here is that the orientation of these stresses are constant to a certain direction unlike the principal stress explained before.

The σ_x magnitude is the largest stress followed by the σ_y and σ_z in the gravity-tectonic scenario. This is due to the σ_x is oriented to N128^{o}E, almost parallel with the direction of the maximum principal stress (N145^{o}E). And at depth 200 m, the largest stress for gravity-tectonic scenarios are the maximum principal stresses. On the other hand, for the gravity-only scenario, the largest stress is the σ_z which oriented normal to the surface. Moreover, In addition, the σ_z magnitude is almost similar throughout the simulation scenarios.

The largest stress on the Figure 30 is the σ_z. It is because at depth 2400 m, the vertical stress becomes more dominant that the horizontal stresses as indicated from the 1D stress analysis. For σ_x and σ_y, the magnitude of these stresses are different in throughout the scenarios. The scenario 4 where the input of tectonic stress is the largest, produces the largest stresses. On the other hand, the scenario 1 where no tectonic stress involved generates the smallest stresses.

The result of 3D geomechanical simulation in cross section 1, 3, and 4 are also indicating the similar result with the cross section 2 both in shallow (200 m) and deep (2400 m) depth. These results can be seen in the Appendix.

The 3D stress model basically is the combination of the acting stress which is also known as the input stress in the previous chapter (1D stress model) with the 3D geological model. The result of the simulation is the stress distribution and can be presented on the principal stress and/or resulting stress in any coordinate system. So here, there are three stress expressions, acting stress, principal stress, and resulting stress and these stresses are different from one another, not only in the magnitude as explained above but also in the direction.

As it can be seen from earlier picture, Figure 24, the direction of the intermediate principal stresses is divided into 3 parts, parallel to the S_{Hmax}, S_{hmin}, and S_v direction (acting stresses). But that is not entirely true since in the transition zone from one part to another part such at the depth 700 m and 1500 m, there are some perturbation of this principal stress direction. It is not parallel but oblique to the acting stress. This was also explained in the chapter 5.3.2.

This perturbation of stress direction is possibly happened because of the effect of the geometry of the model itself such as the curvature of the horizons and faults and also the variation of thickness of each formation/group. But because the effect of the acting stress is much larger than the geometry of the model, mostly the orientation of the principal stresses is the same as the acting stresses.

By knowing the direction and magnitude of the principal stresses within a field, the present-day fault and fracture orientation can be predicted. This knowledge is useful in the several industry that related with subsurface such as oil and gas, geothermal, and CO_2 storage.

5.3.3. 1D and 3D Stress Model Comparison

As it is explained in the 1D stress analysis that from the surface to the bottom of the model, in the gravity-tectonic scenario, the stress regime changes along the depth. Meanwhile, in the gravity-only scenario, the stress regime remains unchanged along the depth. This is due to the effect of the tectonic stress that influence magnitude of horizontal stresses. This is also concluded with the 3D stress analysis in the previous chapter.

However, in 1D model, the stress analysis is not involving the 3D geological model. So that, the magnitude of the stresses are constant throughout the same depth. But actually, in the 3D model, the magnitude of the stresses are different even in the same depth as it can be found in Figure 31.

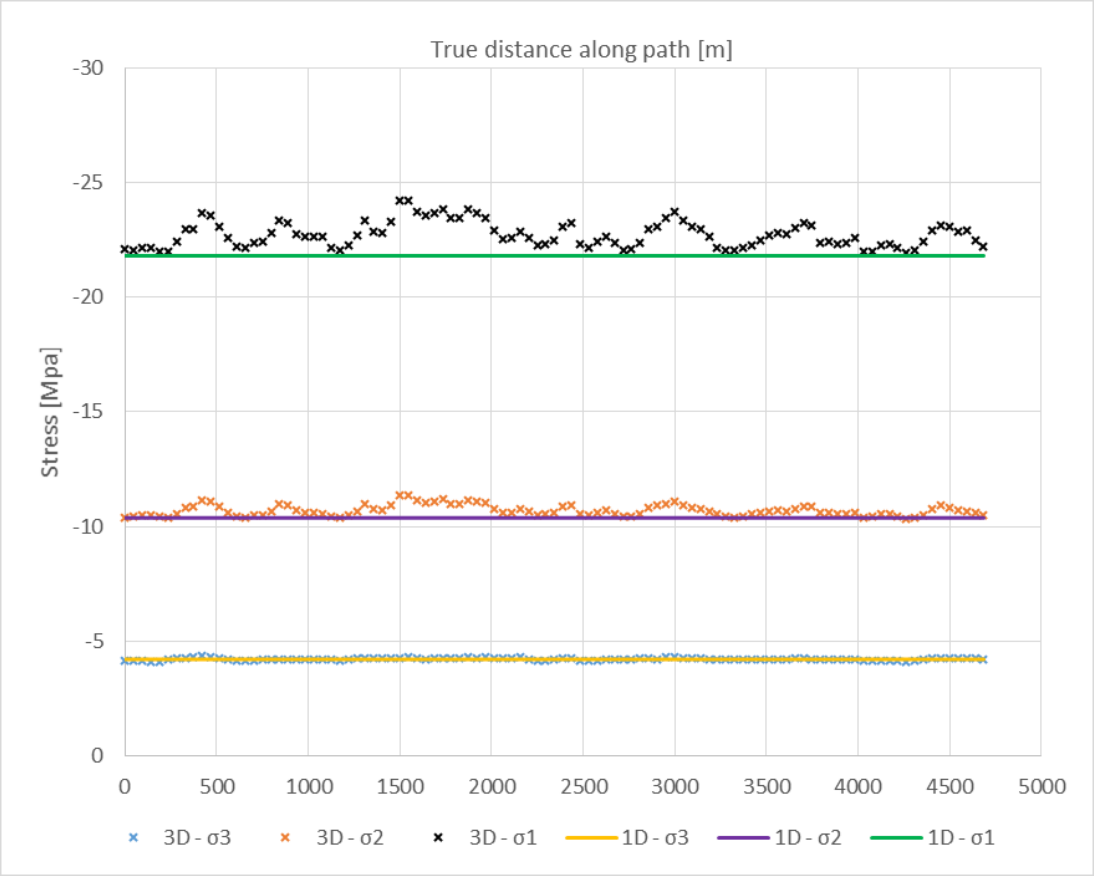

Figure 31. Magnitude of 1D model and 3D model in scenario 3 at cross section 2 depth 200 m.

Figure 31 above is one of the example showing that the 3D stress magnitude is not constant compared with the 1D stress magnitude. This is happened because the 1D stress model is ignoring the 3D geological model thus it does not consider the curvature and the variation of the formation/group thickness from the 3D geological model. Meanwhile, the determination of 3D stress model is involving the 3D geological model. It also indicates that in order to understand the state of stress within an area, the 1D model is not enough and 3D model is needed.

5.3.4. Sensitivity Analysis

The purpose of this analysis is to figure out the effect of the rock properties such as density and Poisson's ratio on the principal stresses along the depth. This sensitivity analysis was conducted by analysing the principal stresses in the reservoir interval at depth 2400 m as an example. The location where the analysis performed was in the middle of cross section 2 (see Figure 26). Scenario 3 had been used as an example which this scenario was including the tectonic stress (20 MPa) as one of the source of the stress.

5.3.4.1. Effect of Density on the Principal Stresses

One of the parameter input for the geomechanical simulation was the density. To examine the effect of the density on the principal stresses in this model, the scenario 3 was assumed to be the base case of the model. The input density for all the stratigraphic units can be seen in Table 9. Three geomechanical simulations were executed with three different density set value, the base case density, 10% larger than base case density, and 10% smaller than base case density.

The result of the simulations using +10% and -10% of the base case density, presented in magnitude of principal stresses is shown in Figure 32. The magnitude principal stresses in this figure are calculated at depth 2400 m.

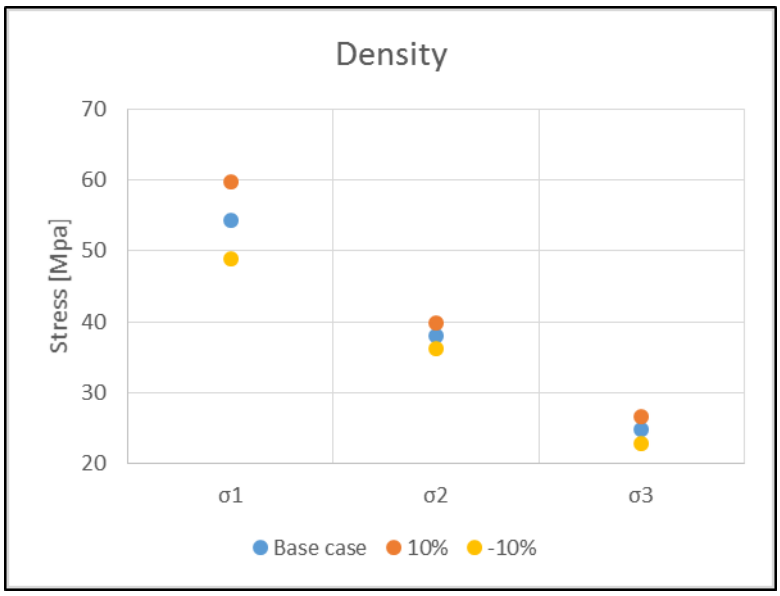

Figure 32. Principal stresses at depth 2400 m with several densities input.

Figure 32 depicts the magnitude of principal stresses result from the different density input mentioned above. The blue dots represent the result of principal stress that using the input density of the base case from Table 9. The orange dots use the 10% larger density values than the base case density. On the other hand, the yellow dots use the 10% smaller density values than the base case density.

It can be seen from this figure that density as one of the input of geomechanical simulation has bigger influence to the maximum principal stress (S_1) at depth 2400 m than the other principal stresses. It is known from the previous chapter, at depth 2400 m, direction of maximum principal stress is vertical. This is reason why the biggest influence of density is to the maximum principal stress. 10% larger or smaller density can change the magnitude of maximum principal stress also ±10% and this changing is considerably large. Meanwhile, the magnitude of minimum principal stress can change ±7.3% and the intermediate principal stress ± 4.8%. The intermediate principal stress has the least affected principal stress by the density. This is because intermediate principal stress from scenario 3 at depth 2400 m is oriented to the direction of S_{Hmax} where the tectonic stress plays a bigger role.

5.3.4.2. Effect of Poisson's Ratio on the Principal Stresses

Another parameter input for the geomechanical simulation was the Poisson's ratio. Same as the density analysis before, to examine the effect of the Poisson's ratio on the principal stresses in this model, the scenario 3 was assumed to be the base case of the model.

The input Poisson's ratio for all the stratigraphic units can be seen in Table 9. Three geomechanical simulations were executed with three different Poisson's ratio set value, the

base case Poisson's ratio, 10% larger than base case Poisson's ratio, and 10% smaller than base case Poisson's ratio.

The result of the simulations using +10% and -10% of the base case Poisson's ratio, presented in magnitude of principal stresses is shown in Figure 33. The magnitude principal stresses in this figure are calculated at depth 2400 m.

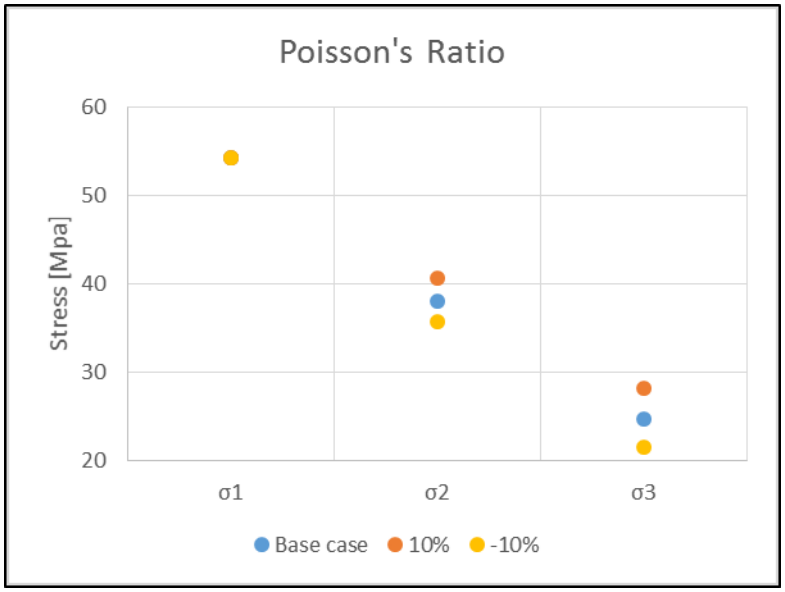

Figure 33. Principal stresses at depth 2400 m with several Poisson's ratios input.

Figure 33 depicts the magnitude of principal stresses result from the different Poisson's ratio input mentioned above. The blue dots represent the result of principal stress that using the input Poisson's ratio of the base case from Table 9. The orange dots use the 10% larger Poisson's ratio values than the base case Poisson's ratio. On the other hand, the yellow dots use the 10% smaller Poisson's ratio values than the base case Poisson's ratio.

The most noticeable feature in this figure is that the changing in Poisson's ratio is not influencing the maximum principal stress (S_1) at this 2400 m depth. This is due to the maximum principal stress at depth 2400 m is oriented to vertical direction which coincides with the vertical stress direction. As it is known that the parameter influencing the magnitude of vertical stress is density and depth.

Another distinguish feature from Figure 33 is that the influence of Poisson's ratio is larger on the minimum principal stress than the intermediate principal stress. 10% different in Poisson's ratio can change the magnitude of minimum principal stress until around 13%. Meanwhile, the effect of changing 10% of Poisson's ratio on the magnitude of intermediate principal stress is only 6% approximately. The estimation of magnitude of the minimum principal stress is important in the determination of mud window for drilling activity.

5.3.5. Stress around the Fault

In order to understand the effect of the fault in to the stress within the model, calculating the stress around the faults was performed. The analysis was conducted by analysing the principal stress in the cross section number 2 (see Figure 26) at depth 1800 m. The selection of this depth was because at this depth, there were two faults that can be observed so that the stress magnitude around those faults can be calculated.

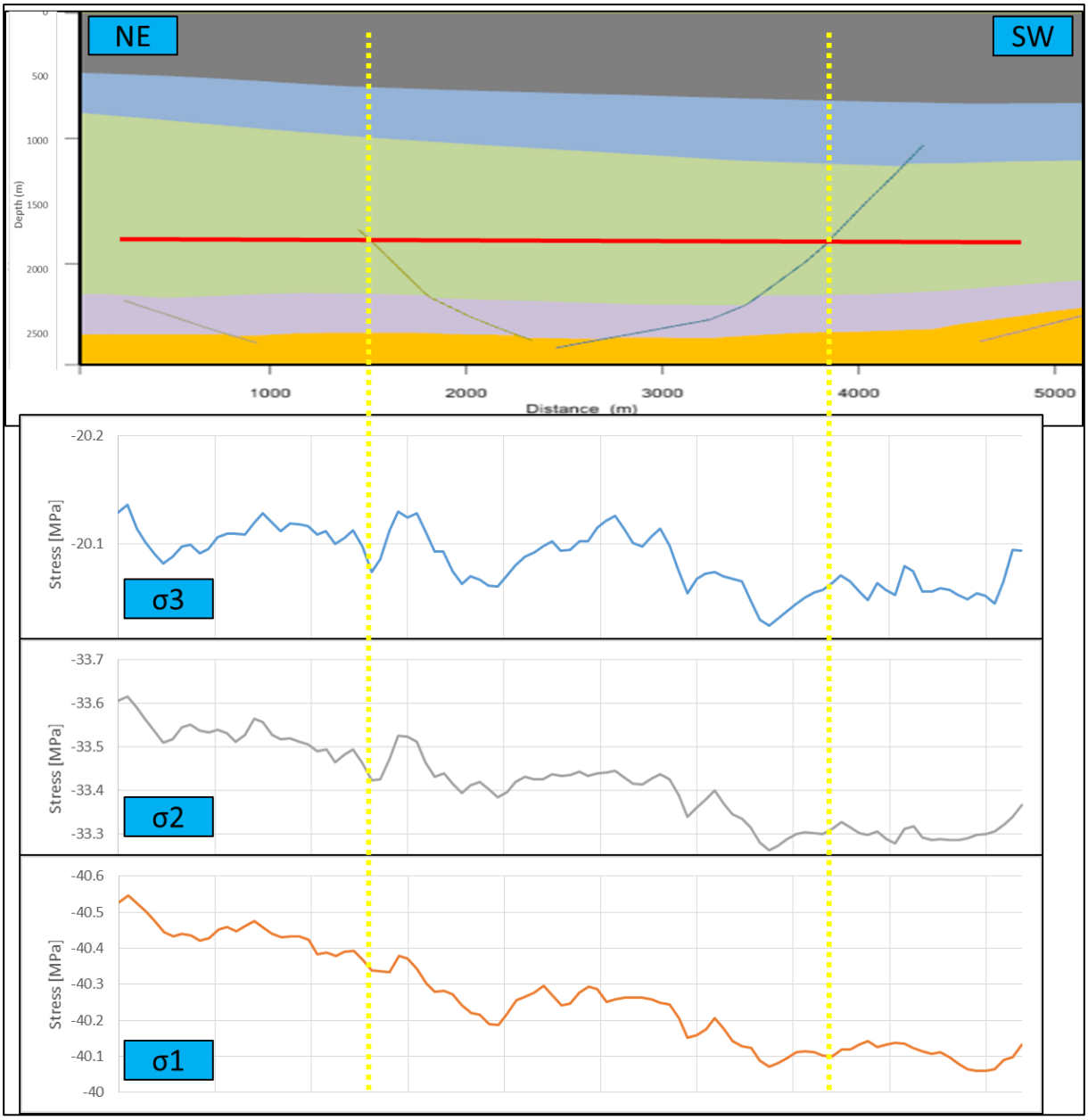

Figure 34. Principal stresses (graphs) calculated along the red line (in the cross section 2).

Figure 34 depicts the graph of all principal stresses against the distance along the red line. The yellow-dashed lines show the location of the faults correspond to the magnitude of all the principal stresses. Two faults are observed in this figure. The principal stresses on these faults compared to their surroundings show insignificant changes in magnitude. Although, the fault on the left hand side of the figure indicates a decrease in magnitude than its surroundings, the depression is not considered large. On the other hand, the fault on the right hand side of the figure is not showing any major difference with its surroundings.

To sum up, the presence of the fault in the model is not significantly effecting the magnitude of all principal stresses. However, it still can affect the magnitude of principal stresses though it

is very small magnitude. This is due to the fact that in this model, the faults are set to be fixed and cannot moving. They are only the part of the geometry of the model. And also because the material properties on hanging wall and the foot wall of each faults are the same since they are on the same stratigraphic unit.

5.3.6. Pore Pressure Effect

The assumption made for the models in this study is zero pore pressure for the sake of simplicity. But in the reality, the rocks especially the sedimentary rock has pore space and fluid inside. In this part, the difference of result between using the zero pore pressure and hydrostatic pore pressure is analysed. The scenario 2, the gravity-tectonic scenario with tectonic stress equals to 10 MPa is using to execute this analysis.

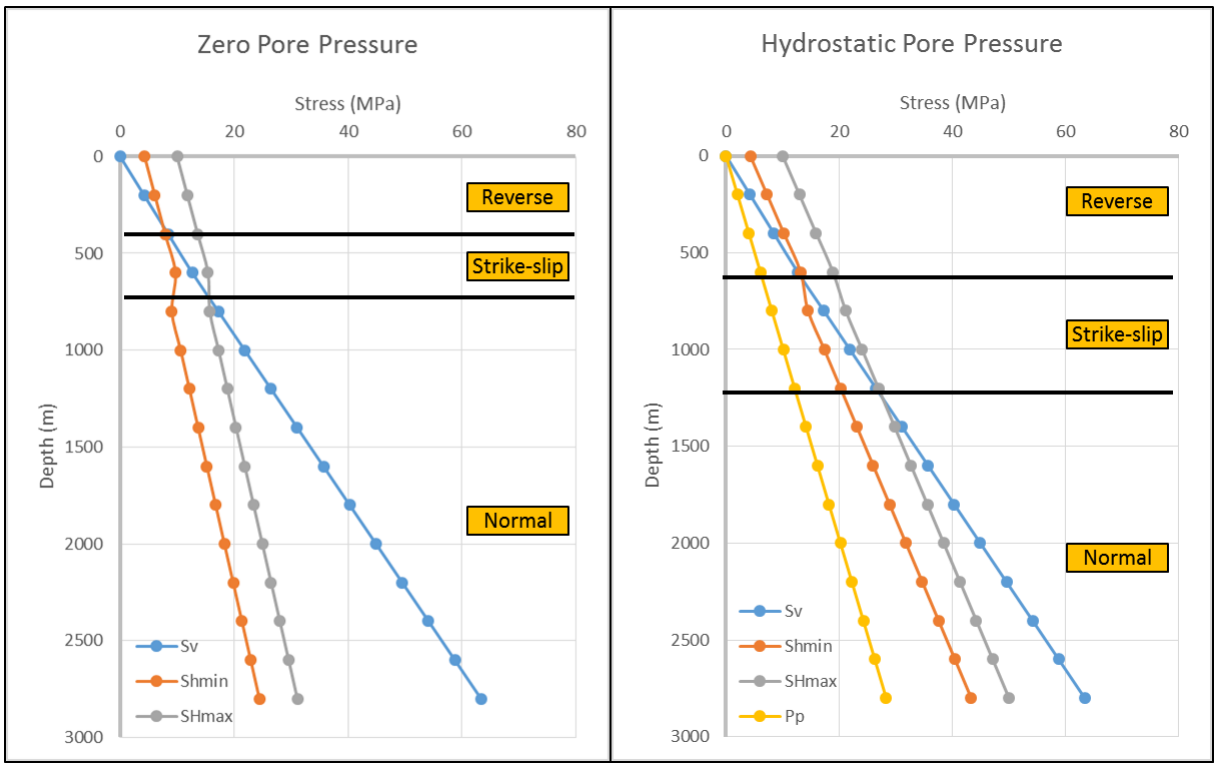

Figure 35. Comparison of 1D stress result between zero pore pressure (left) and hydrostatic pore pressure (right).

Figure 35 illustrates the comparison between the 1D stress result in the case with hydrostatic pressure and zero pore pressure. All the parameter inputs for both cases are the same. The only difference is only the magnitude of the pore pressure.

On this figure, it can be seen that the magnitude of vertical stress in both cases is the same but not with the horizontal stresses. The gradient of horizontal stresses on the zero pore pressure case is smaller than on the hydrostatic pore pressure case. This causes the difference in the thickness of each stress faulting regime. For instance, in the zero pore pressure case, the reverse and strike-slip faulting regime zone are thinner than in the case of hydrostatic pore pressure.

In the zero pore pressure case, the orientation of maximum principal stress (S_1) is to the direction of S_{Hmax} until depth around 750 m and below 750 m, the orientation of S_1 is to vertical stress direction. Meanwhile, in the hydrostatic pore pressure case, the orientation of S_1 to the direction of S_{Hmax} is even deeper until the depth around 1250 m. This indicates that the presence of the pore pressure is affecting the orientation of principal stress and its faulting regime.

Another difference between the results of these two cases is that the effective stresses in the zero pore pressure case is higher than the effective stress from hydrostatic pore pressure.

Since in the zero pore pressure case, the effective stress equals to total stress but in the hydrostatic pore pressure case, the effective stress equals to total stress minus pore pressure.

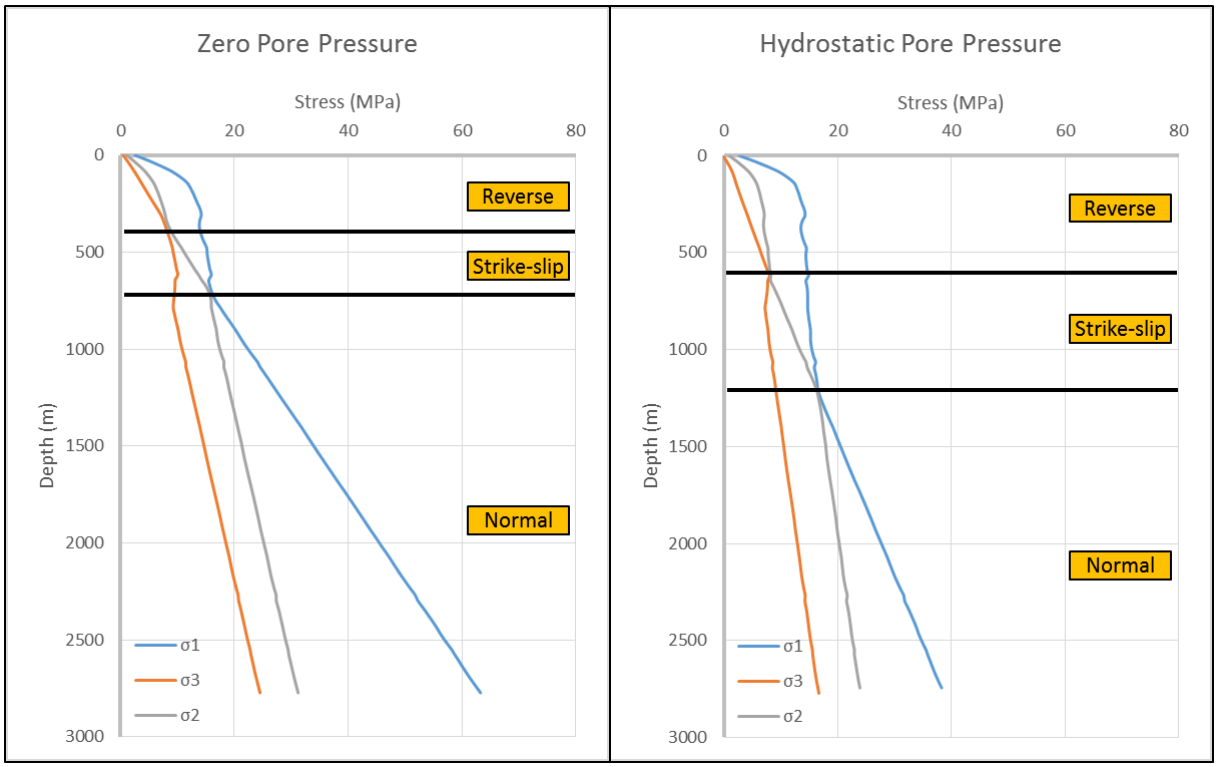

Figure 36. Comparison of 3D stress result between zero pore pressure (left) and hydrostatic pore pressure (right).

Figure 36 depicts the 3D stress result, presented on principal stresses, between the zero pore pressure case and hydrostatic pore pressure case. The thickness of the reverse and strike-slip faulting regime zone are bigger in the hydrostatic pore pressure case than in the zero pore pressure case. This result is quite similar with the 1D stress result.

Since the pore pressure in the hydrostatic pore pressure case is higher than the zero pore pressure case, magnitude of principal stresses in the hydrostatic pore pressure case is smaller than in the zero pore pressure. Because the principal stresses has taking into account the magnitude of the pore pressure just like the calculation of the effective stress. This is similar to the result of the effective stress magnitude comparison in the 1D stress result where the effective stress in the hydrostatic pressure is smaller than the effective stress in the zero pore pressure.

The effect of the pore pressure in the drilling activity is important. For instance, in the activity of fluid injection for EOR, the pore pressure is increasing. Thus, it could lead to the creation of a new set of fracture/fault or reactivation of the existing fracture/fault if the pore pressure is too large. On the other hand, for example on the reservoir depletion, the pore pressure is decreasing. This could lead ground subsidence to be occurred if the pore pressure is small.

6. Conclusion and Recommendation

The 3D geomechanical model has been successfully established by applying the acting stress on the 3D geological model. The size of the 3D geological model is approximately 9.7 km x 5.2 km with the deepest depth at 2.8 km and has been built using the seismic and well data. By building the 3D geomechanical model, the 3D stress distribution within the De Lier field can be identified. This 3D geomechanical model have 4 scenarios by varying the magnitude of tectonic stress. One scenario only includes the overburden rock and gravity without tectonic stress as the source of stress scenario. Meanwhile, the other three scenarios also includes the tectonic stress. In these gravity-tectonic scenarios, the tectonic stresses are applied as an external source of stress and the magnitude vary from 10, 20, and 30 MPa.

The output of this 3D stress distribution can be visualized on the principal coordinate system and in any arbitrary Cartesian coordinate system. In the principal coordinate system, the direction and magnitude of principal stresses can be extracted. On the other hand, in the Cartesian coordinate system, the magnitude of the resulting stress to the certain direction can be obtained.

From the gravity-only scenario, there is only one stress regime from the whole depth of the model, normal stress regime where the vertical stress becomes the maximum principal stress. In the gravity-tectonic scenarios, the stress regimes are varying from the top to the bottom of the model. In the shallower part of the model, the vertical stress becomes the minimum principal stress while in the deeper part, it becomes the maximum principal stress.

The 1D stress model is basically is the stress input for the 3D stress modeling. However, the 1D stress model did not consider the 3D geological feature and structure such as horizons and faults in its calculation. Therefore, the stresses are constant throughout the model at the same depth. In contrast, in the 3D stress modeling, it is considering the architecture of the 3D geological model. Thus, the stress magnitudes are not constant but fluctuate throughout the model and the direction of the principal stresses are not always parallel with the acting stress (given stress). Some perturbations are occurred in the transition zone between the stress regimes. Indeed, the architecture of the model is influencing the stress result in terms of magnitude and orientation. But the effect of the curvature of the horizons and faults is not as large as the effect of the applied stress. Therefore, the main orientation of the principal stresses are still parallel to the applied stresses.

Density and Poisson's ratio are two main parameter inputs for the stress calculation. By changing the density ±10% from the base case, it can influence the result of the σ_1 ±10% at depth 2400 m. It also influences the other principal stress but not as large as the σ_1. On the other hand, by changing the Poisson's ratio ±10% from the base case, the principal stress magnitude at depth 2400 m are changing but not the σ_1. The σ_3 is the most principal stress affected by the Poisson's ratio. In addition, the magnitude of the pore pressure can influence the principal stresses, effective stress, and the thickness of the stress regime zone. As the pore pressure becomes higher, the principal and effective stress become smaller. On the contrary, the thickness of the stress regime zone is larger in the higher pore pressure.

The usefulness of the 3D geomechanical model can be applied to many industries related with the subsurface such as oil and gas, geothermal, and CO_2 storage even in the geotechnical engineering. It is very useful mainly in the fluid injection, subsidence, fault reactivation, and wellbore stability study.

The 3D geomechanical model in this study can be improved by adding the wellbore breakout and induced fracture data in order to get the more realistic orientation of horizontal stresses. The picked horizons and fault from seismic data as the input for geological model generation can be enhanced in terms of accuracy and precision by gathering more data such as check-shot data and advanced velocity modeling data. Since the stress regime within an area influences the generation of the geological structure, study about the outcrop and fracture modeling are needed to give the confirmation of the result.

References

Abaqus 6.12 Analysis User's Manual. (2012). Dassault Systemes.

Bertotti, G., Graaf, S. d., Bisdom, K., Oskam, B., Vonhof, H. B., Bezerra, F. H., . . . Cazarin, C. L. (2017). Fracturing and fluid-flow during post-rift subsidence in carbonates of the Jandaira Formation,Potiguar Basin,NE Brazil. *Basin Research, John Wiley & Sons Ltd, European Association of Geoscientists & Engineers and International Association of Sedimentologists*. doi:10.1111/bre.12246

Brown, E. T., & Hoek, E. (1978). Trends in relationship between measured in-situ stresses and depth. *Int. J. Rock Mech. Min. Sci. & Geomech.*, 211-215.

DeVault, B., & Jeremiah, J. (2002). Tectonostratigraphy of the Nieuwerkerk Formation (Delfland subgroup), West Netherlands Basins. *AAPG Bulletin, v.86, No. 10*, 1679–1707.

Donselaar, M. E., Groenenberg, R. M., & Gilding, D. T. (2015). Reservoir geology and geothermal potential of the Delft Sandstone Member in the West Netherlands Basin. *World Geothermal Congress 2015.* Melbourne.

Duin, E., Doornenbal, J., Rijkers, R., Verbeek, J., & Wong, T. E. (2006). Subsurface structure of the Netherlands – results of recent onshore and offshore mapping. *Netherlands Journal of Geosciences - Geologie En Mijnbouw*, 245-276.

Eaton, B. A. (1969). Fracture gradient prediction and its application in oilfield operation. *Journal of Petroleum Technology, Vol. 21*, 1353-1360.

Fisher, K., & Henk, A. (2013). A workflow for building and calibrating 3-D geomechanical models – a case study for a gas reservoir in the North German Basin. *Solid Earth*.

Heidbach, O., Rajabi, M., Reiter, K., & Ziegler, M. (2016). World Stress Map 2016. GFZ Data Service. doi:10.5880/WSM.2016.002

Jaeger, J. C., Cook, N. G., & Zimmerman, R. W. (2007). *Fundamentals of rock mechanics, 4th ed.* Blackwell.

Jager, D. d. (1996). Fluviomarine sequences in the Lower Cretaceous of the West Netherlands Basin: correlation and seismic expression. In H. Rondeel, D. Batjes, & W. Nieuwenhuijs, *Geology of gas and oil under the Netherlands* (pp. 229-241). Springer Netherlands.

Jones, C. K. (2016). *Multi-scale fault network characterization of West Netherlands Basin from 3D seismic horizon maps.* Delft: TU Delft.

Muller, B., Zoback, M. L., Fuchs, K., Mastin, L., Gregersen, S., Pavoni, N., . . . Ljunggren, C. (1992). Regional pattern of tectonic stress in Europe. *Journal of Geophysical Research, Vol. 97*, 11,783-11,803.

Price, N. J. (1966). *Fault and joint development in brittle and semi-brittle rock.* Pergamon Press.

Ranjan, S. (2015). *Mechanical modelling of the stress state in a reservoir-scale fold during and after folding.* Delft: TU Delft.

Ranjbar, A., Hassani, H., & Shahriar, K. (2017). 3D geomechanical modeling and estimating the compaction and subsidence of Fahlian reservoir formation (X-field in SWof Iran). *Arab J Geosci*.

Ros, J. F. (2016). *Qualitative Analysis on Fault Fabrics extracted from the West Netherlands Basin relevant for Geothermal Application.* Delft: TU Delft.

Shearer, P. M. (2009). *Introduction to seismology, 2nd ed.* New York: Cambridge University Press.

Taylor, R. G., Steehouwer, M., Turmaine, B., & van Ratingen, S. (2016). *JewelSuite 6.2 Subsurface Modeling User Manual.* Baker Hughes.

(2013). *Technical addendum to the Winningsplan Groningen 2013 subsidence, induced earthquakes and seismic hazard analysis in the Groningen Field.* NAM.

Terzaghi, K. (1943). *Theoretical soil mechanics.* New York: John Wiley.

TNO, Geological Survey of the Netherlands. (n.d.). *Models, maps and datasets*. Retrieved from NLOG: http://nlog.nl/en/models-maps-and-datasets

Van Adrichem Boogaert, H., & Kouwe, W. (1993-1997). *Nomenclature (Deep)*. Retrieved from Dinoloket: https://www.dinoloket.nl/nomenclature-deep

van den Bogert, P., van Elk, J., & Doornhof, D. (2015). *Impact of various modelling options on the onset of fault slip and the fault slip response using 2-dimensional Finite-Element modelling.* NAM.

van der Zee, W., Ozan, C., Brudy, M., & Holland, M. (2011). 3D Geomechanical modeling of complex salt structure. *SIMULIA Customer Conference*.

van Eijs, R., van Elk, J., & Doornhof, D. (2015). *Neotectonic stresses in the Permian Slochteren Formation of the Groningen Field.* NAM.

Vis, G.-J., van Gessel, S., Mijnlieff, H., Pluymaekers, M., Hettelaar, J., & Stegers, D. (2010). *Lower Cretaceous Rijnland Group aquifers in the West Netherlands Basin: suitability for geothermal energy.* Utrecht: TNO.

Walter, F. (1995). The status of geothermal energy in the Netherlands. *World Geothermal Congress*, (pp. 279-281). Florence.

Wiggers, C. (2009). *The Delft Sandstone in the West Netherlands Basin.* Delft: TU Delft.

Wong, T. E., Batjes, D. A., & Jager, J. D. (2007). *Geology of the Netherlands.* Amsterdam: Royal Netherlands Academy of Arts and Sciences.

Zoback, M. D. (2007). *Reservoir Geomechanics.* New York: Cambridge University Press.

Zoback, M. D., Barton, C., Castillo, D., Finkbeiner, T., Grollimund, B., Moos, D., . . . Wiprut, D. (2003). Determination of stress orientation and magnitude in deep wells. *International Journal of Rock Mechanics & Mining Sciences 40*, 1049-1076.

Zoback, M. L. (1992). First- and second-order of stress in the Lithosphere: the world stress map project. *Journal of Geophysical Research, Vol. 97*, 11,703-11,728.

Appendix A – Principal Stresses of 3D Stress Model in Cross Section 1, 3, and 4

Cross section 1 (200 m)

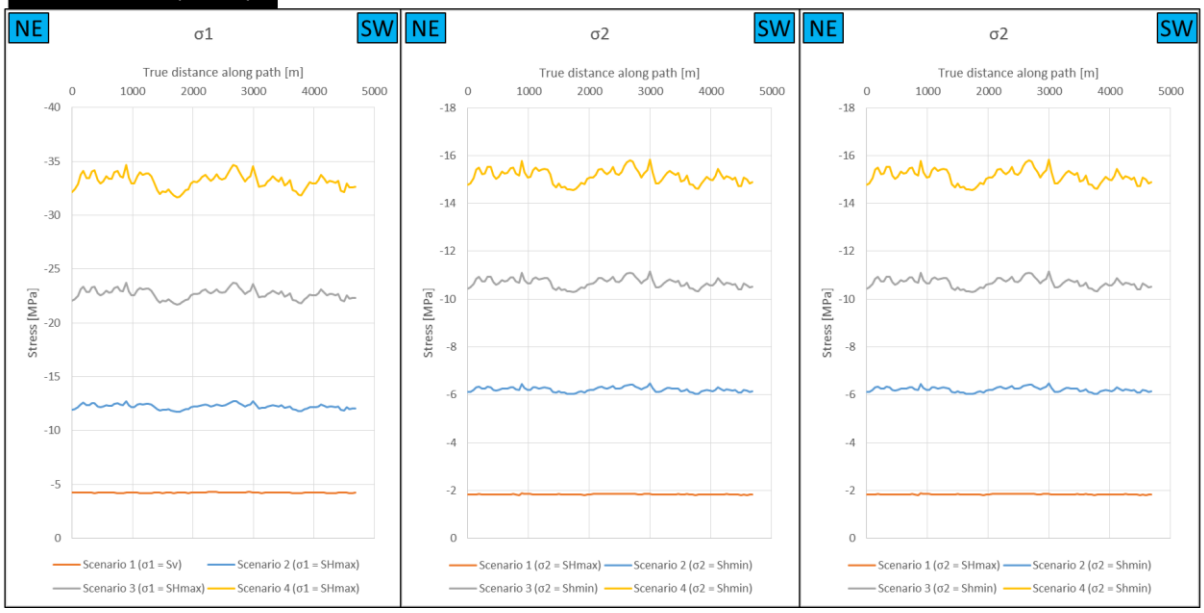

Cross section 1 (2400 m)

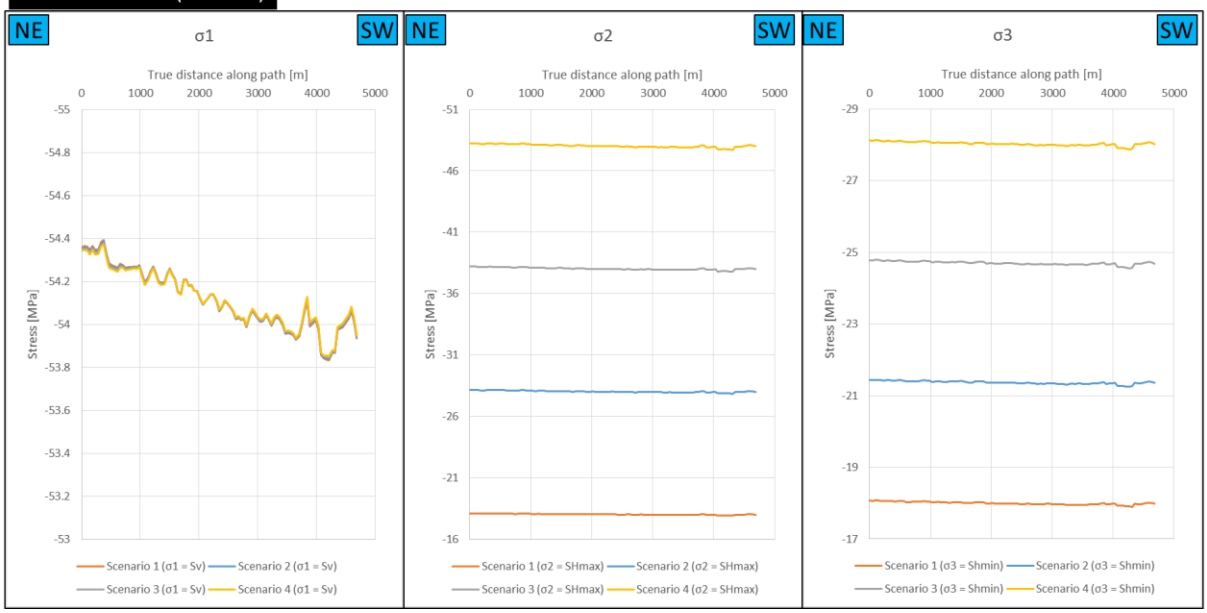

Cross section 3 (200 m)

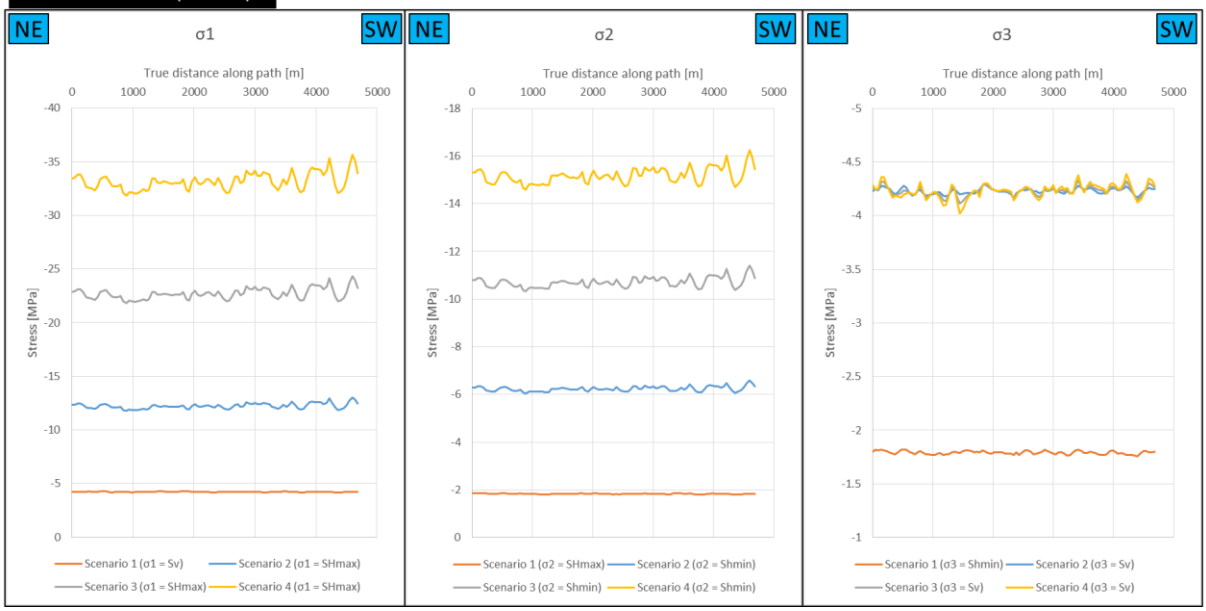

Cross section 3 (2400 m)

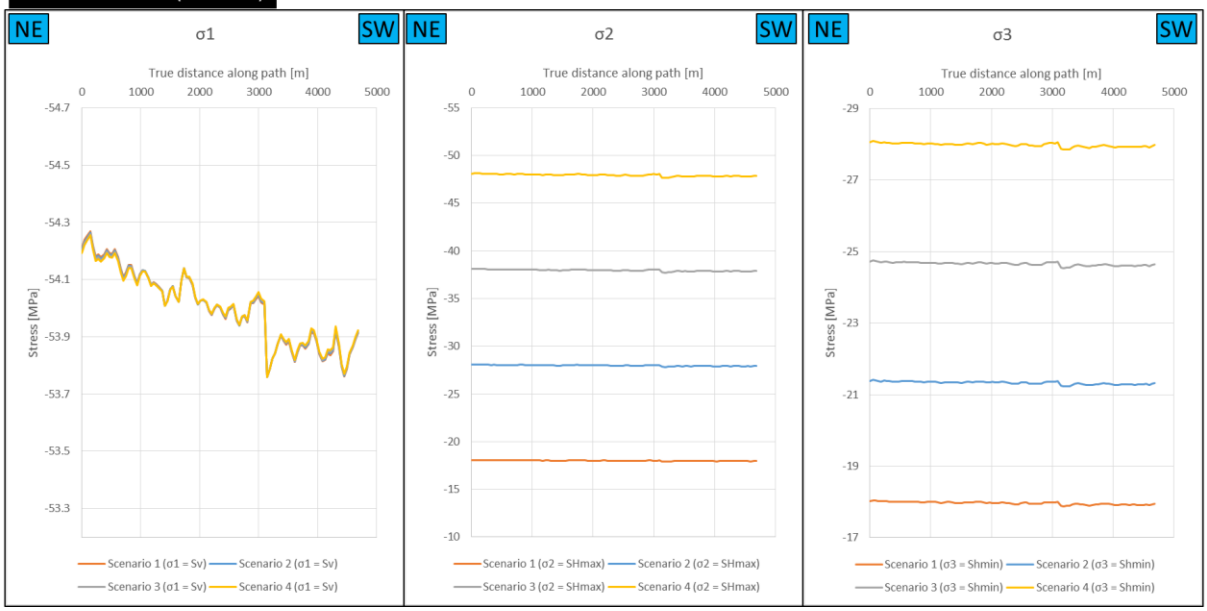

Cross section 4 (200 m)

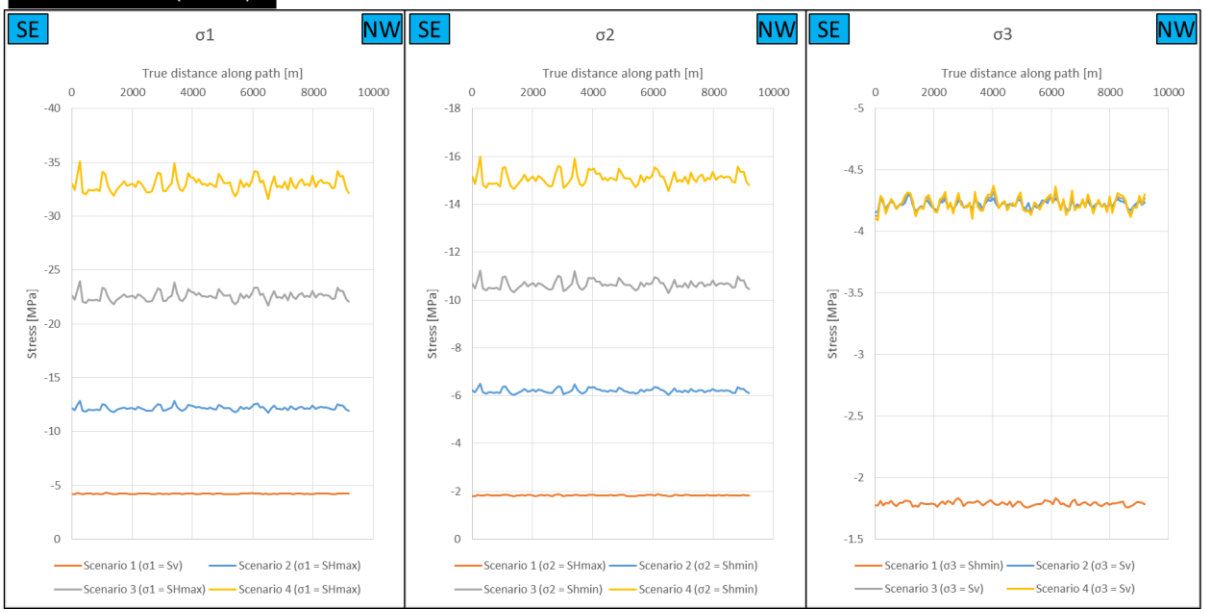

Cross section 4 (2400 m)

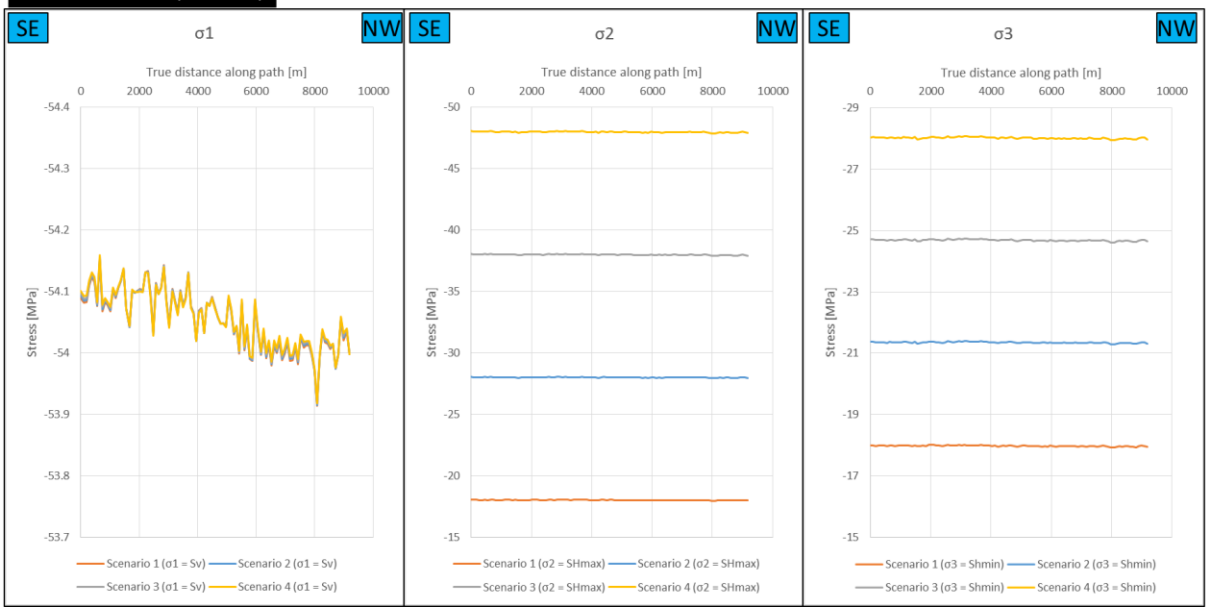

Appendix B – Resulting Stresses of 3D Stress Model in Cross Section 1, 3, and 4 at x, y, and z-direction

Cross section 1 (200 m)

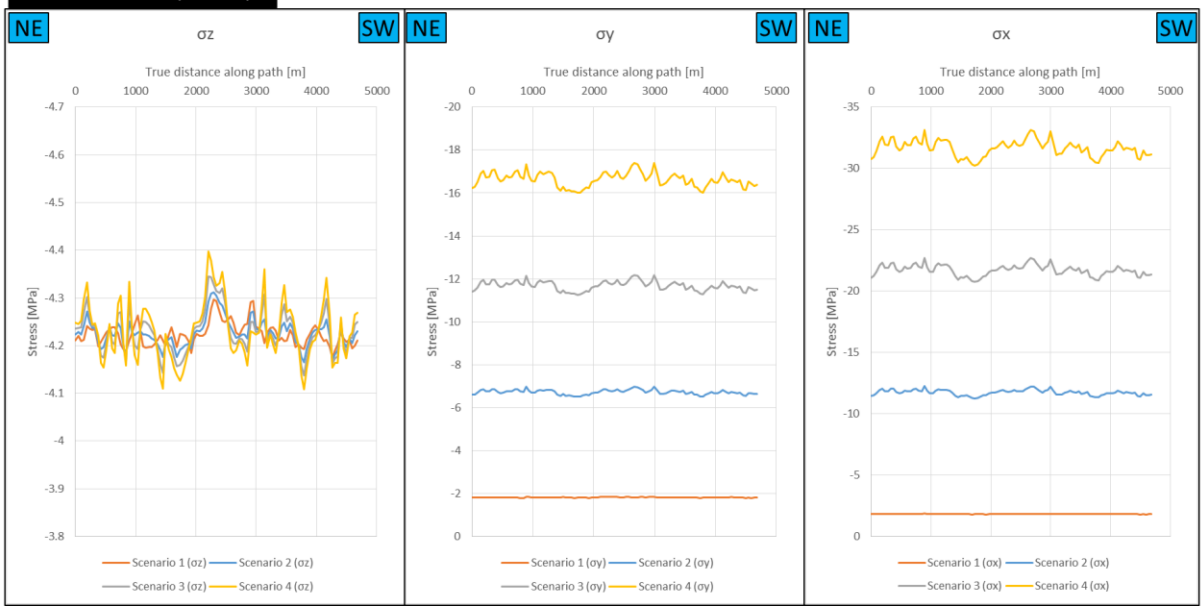

Cross section 1 (2400 m)

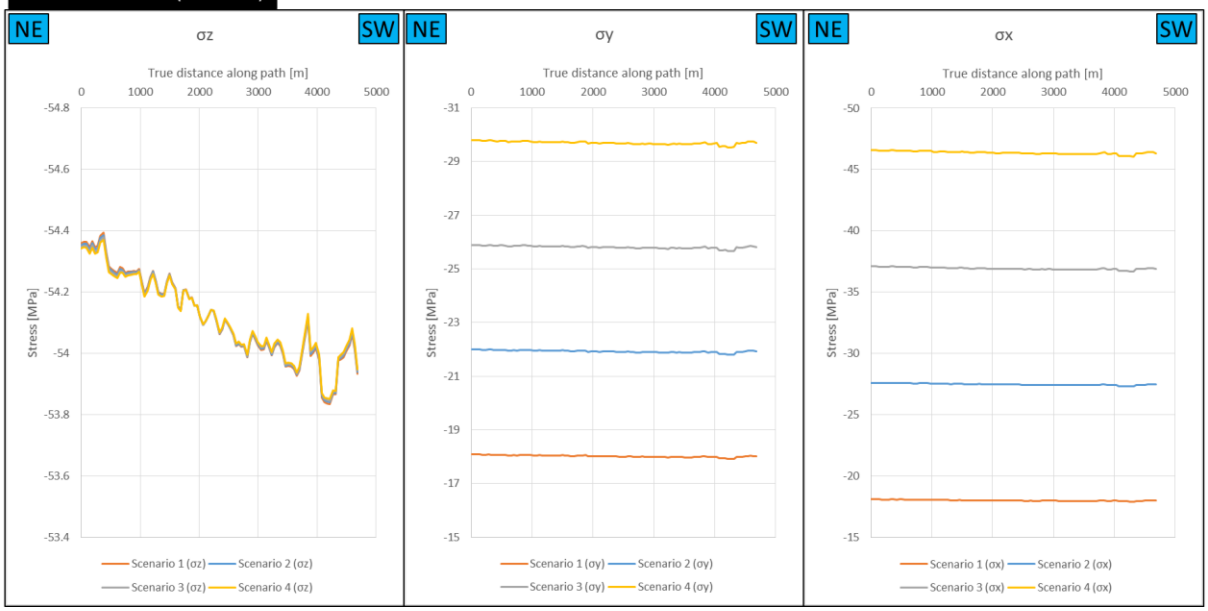

Cross section 3 (200 m)

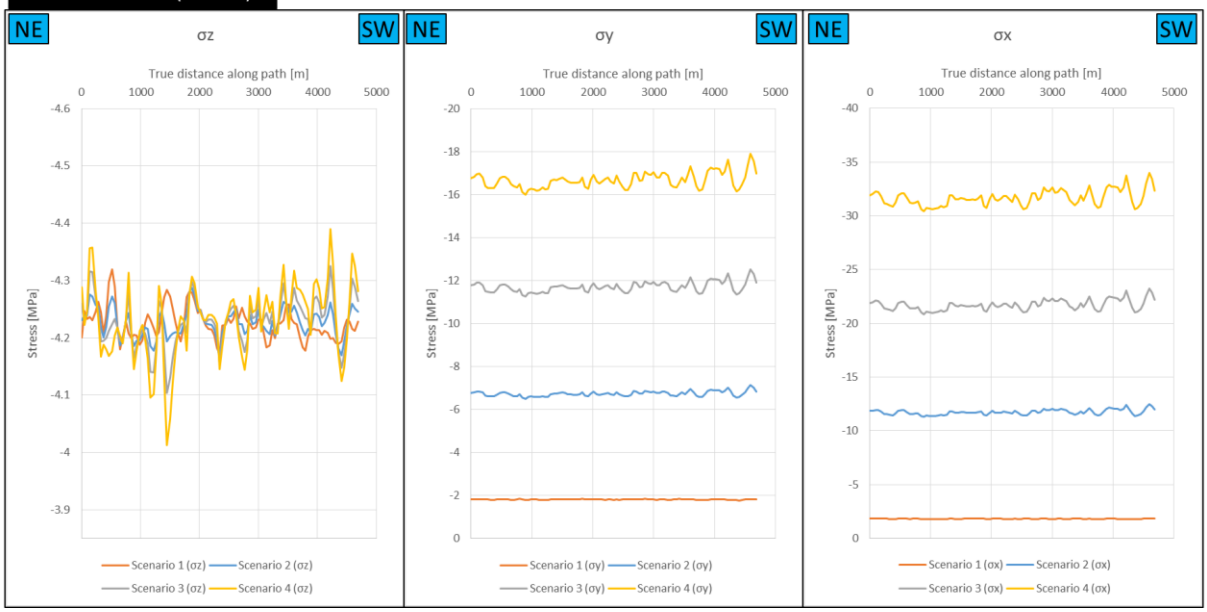

Cross section 3 (2400 m)

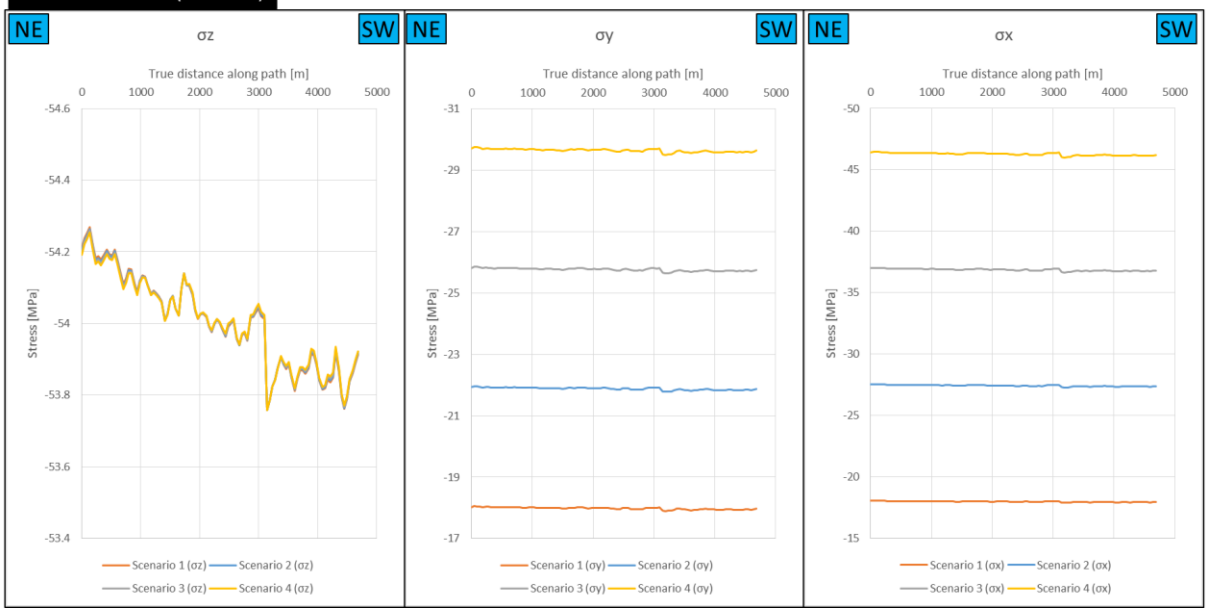

Cross section 4 (200 m)

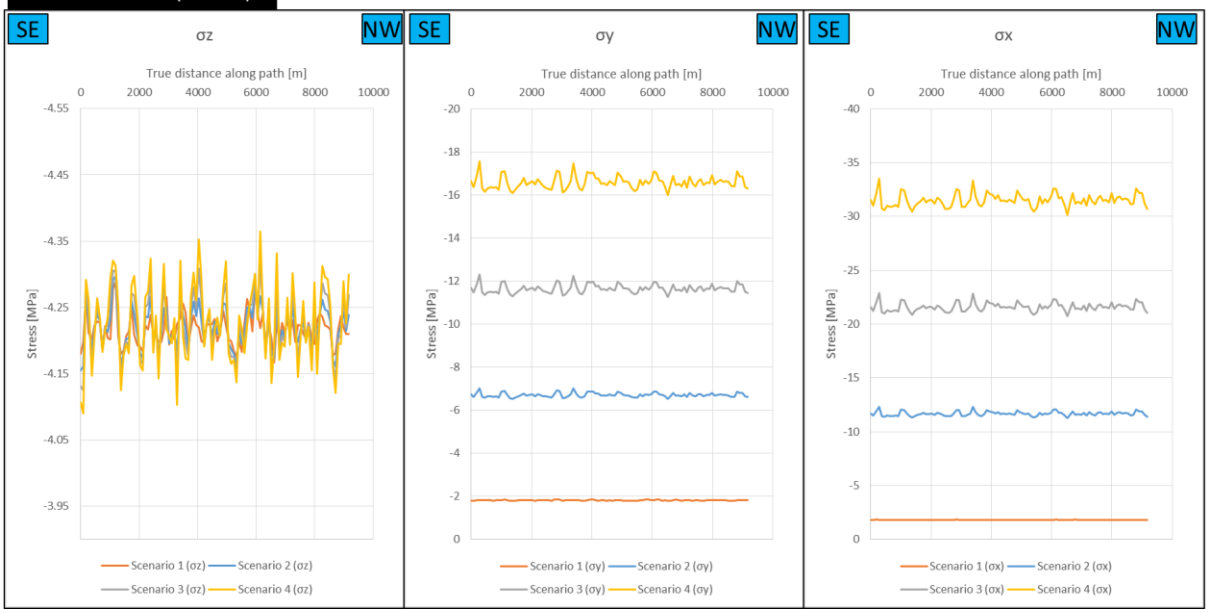

Cross section 4 (2400 m)